PREDICTING THE HYDRODYNAMIC ACOUSTIC SIGNATURE OF CFAV QUEST IN THE NEAR SURFACE ENVIRONMENT

by

Robert Doyle

Submitted in partial fulfillment of the
requirements for the degree of
Master of Applied Science

at

Dalhousie University
Halifax, Nova Scotia
September 2012

DALHOUSIE UNIVERSITY

DEPARTMENT OF MECHANICAL ENGINEERING

The undersigned hereby certify that they have read and recommend to the Faculty of Graduate Studies for acceptance a thesis entitled "PREDICTING THE HYDRODYNAMIC ACOUSTIC SIGNATURE OF CFAV QUEST IN THE NEAR SURFACE ENVIRONMENT" by Robert Doyle in partial fulfillment of the requirements for the degree of Master of Applied Science.

Dated: September 21, 2012

Co-supervisors: _____
Dr Julio Miltizer

_____
Dr Mae Seto

Readers: _____
Dr Robert Bauer

_____
Dr Serguei Iakovlev

DALHOUSIE UNIVERSITY

DATE: September 21, 2012

AUTHOR: Robert Doyle

TITLE: PREDICTING THE HYDRODYNAMIC ACOUSTIC SIGNATURE OF CFAV QUEST IN THE NEAR SURFACE ENVIRONMENT

DEPARTMENT OR SCHOOL: Department of Mechanical Engineering

DEGREE: M.A.Sc. CONVOCATION: May YEAR: 2013

Signature of Author

Table of Contents

List of Tables

List of Figures

Abstract

Three models for the generation and propagation of hydrodynamic noise near the ocean surface are presented, and are compared for their ability to predict hull noise generated by CFAV Quest. The simulated fluctuating pressure field on the hull is also validated against experimental results. The near field flow is first solved using the NWT CFD package, and the hydrodynamic noise is calculated using the Lighthill-Curle acoustic analogy. The far field sound is obtained using three methods: a method of images solution to the Lighthill-Curle equations, a simple source model of the transmission loss, or a normal mode model of the transmission loss. Both the simple source and method of images models improve the SPL predictions of the Lighthil-Curle equations. Best performance is obtained from the method of images, improving predictions by approximately 40 dB. The normal mode model is shown to give poor results, due to assumed sea-floor boundary conditions.

List of Abbreviations and Symbols Used

$H_0^{(1)}$	0^{th} order Hankel function of the first kind
δ_{ij}	Dirac's delta
λ	Acoustic wavelength
ω	Radial frequency
ρ	Density
ρ_0	Reference density
u_0	Reference velocity
u_i	Velocity in direction i
D	Channel depth
Fr	Froude number
I	Acoustic intensity
M	Mach number
R_i	Propagation path length
Re	Reynolds number
S	Surface area
St	Strouhal number
T_{ij}	Lighthill's Stress Tensor
V	Volume
Φ	Range function
Ψ	Depth function
$\eta_{acoustic}$	Acoustic efficiency
γ	Bi-linear gradient tuning constants
ξ^2	Mode number
a_0	Ambient speed of sound
c	Local speed of sound
f	Frequency
h	Vertical mesh width
k	Wavenumber

l_0	Reference length
l_e	Turbulent eddy size
l_i	Outward normal in direction i
n	Outward normal vector
p	Pressure
p_0	Reference pressure
p_{ij}	Pressure tensor
r	Horizontal range or radial distance
t	Time
x_i	Position in direction i
z	Observer depth
z_s	Source depth

BLS	Baldwin-Lomax-Smagorinsky

CFAV	Canadian Forces Auxillary Vehicle
CFD	Computational Fluid Dynamics

DNS	Direct Numerical Simulation
DP	Direct Path
DRDC	Defense Research and Development Canada

LES	Large Eddy Simulation

NWT	Numerical Wind Tunnel

RANS	Reynolds Averaged Navier-Stokes

SGS	Sub-Grid Scale
SONAR	Sound Navigation And Ranging

SPL Sound pressure level

SRP Surface Reflected Path

STL Stereolithography file

TL Transmission Loss

Acknowledgements

This work was made possible by the generous support of Defense Research and Development Canada, Atlantic, and Dalhousie University, for which both of these institutions have my deepest gratitude. I would like to further thank all my peers, friends and family for all of their support, especially Rachel Wise, Andrew Clarke, Dr Rishad Irani, Al-Mokhtar Mohamed, Andrew Cameron and countless others. Finally, I would like to thank my supervisors, Dr Julio Militzer and Dr Mae Seto, for everything they've taught me, and having the patience and dedication to guide me through every stage of my research. Their support more then anything else is what has made this work possible.

Chapter 1

Introduction

In the design of ocean going vessels, and military craft in particular, acoustic performance is a critical factor. In the marine environment, the attenuation of light and radio waves is much higher than that of sound waves, and acoustics therefore rises in importance as one of the primary sensor mediums. Acoustic factors will impact a variety of ship systems, including sensors and detection, communication, and stealth operations. Knowledge of the noise a ship creates during operation is therefore critical for the successful operation of many vessels.

The unique sound profile of a ship in operation is referred to as the ship's acoustic signature. It has many contributing factors, including but not limited to ship-board machinery, cavitation around propellers, crew operations, the flexing of hull plates and members, and hydrodynamic hull noise. Hydrodynamic hull noise is the sound created by fluid flow along a rigid ship hull, and it is this noise source on which this study focuses. Hull noise is not a major contributing factor to a ship's radiated acoustic signature, which is typically negligible compared to machinery and propeller noise, however it is important in specific contexts. The ship's SONAR (sound navigation and ranging) dome will be especially sensitive to hull noise. Located on the bow of the ship, ahead of the machinery and propellers which dominate the radiated signature, the sonar dome will hear primarily hear the noise generated in the bow of the ship. This bow noise will form the limits of the sonar domes detection envelope; in order to truly detect a signal, the SONAR dome must be able to separate it from the background noise. At the bow of the ship, the hydrodynamic hull noise will be a significantly greater contributor to the signature heard at the SONAR dome, and is therefore critical for good SONAR performance.

Hydrodynamic hull noise is generated by the motion of any rigid body traveling through fluid. Disturbances caused by turbulence within the boundary layer region along the ships hull will cause fluctuations in pressure and stress, which will radiate

away from the ship as sound. The character of this sound is affected by several parameters including the ships velocity, ambient conditions, and hull geometry. Due to its intimate link with fluid turbulence, a difficult and poorly understood phenomenon itself, hydrodynamic hull noise is relatively poorly studied in comparison to other noise sources. By borrowing techniques developed by the field of computational aero-acoustics, it is possible to accurately simulate and predict hull noise based on operating conditions and CAD models of the ship's hull. Computational methods provide a powerful tool for research and investigation of hydrodynamically produced sound, and the insights gained from these models will lead to a greater understanding, and ultimately control, of this portion of a ships acoustic signature.

1.1 Literature Review

Computational aero-acoustics is a quickly growing field that has developed a number of approaches to the problem of noise generation by fluid flow. While originally developed for aerospace applications, the equations and methods are adaptable to use in a variety of conditions, including simulations of wind turbines, race cars, and even watercraft (in the application of which it is referred to as computational hydro-acoustics). These approaches will vary greatly in their complexity and cost, both in terms of time and computer power. What follows is a review of some, but by no means all, of the simulation methodologies utilized in flow noise problems.

Hull noise is generated and propagated by effects routed purely in fluid dynamics, and it would follow that it is possible to simulate and predict it using the methods and tools of computational fluid dynamics, or CFD. It is theoretically possible to discretely solve the compressible fluid flow equations on a grid accurate enough to reproduce the pressure and density fluctuations that make up sound, however in practice this approach is a poor and often unfeasible option. The conversion from fluid flow energy to acoustic energy is very inefficient; the vast majority of the energy remains in the fluid flow. For flows of low Mach number, the efficiency of transfer is proportional to the fourth power of the Mach number, $\eta_{acoustic} \propto M^4$ [8]. Additionally, the wavelength of sound produced in a flow will be proportional to the ratio of eddy size l_e to Mach number, $\lambda \propto \frac{l_e}{M}$ [16]. This ratio leads to a large disparity in scale between the salient features of the flow field and those of the sound field. These

effects combine to require a prohibitively fine grid on which to discretize the equations. Accurately including the turbulence effects that create the noise is a further complication, as turbulence modeling in CFD is itself a developing field. Directly solving for the turbulent motions adds further strict requirements into the discretization and is currently limited to flows of prohibitively low Reynolds number[30]. While a direct solution of the Navier-Stokes equations would be the most physically correct approach, such a solution is technologically un-feasible for the problem at hand.

The alternative strategy typically is to split the problem into two. The fluid flow of interest is first solved using CFD procedures utilizing either direct numerical simulation (DNS) of turbulence or turbulent modeling. While acoustics is technically a compressible flow phenomenon, work by Ask et al [4] has shown that in flows of low Mach number, the incompressible fluid flow equations may be used to evaluate the flow features of the source terms with negligible error in subsequent acoustic predictions. From the resulting flow field, acoustic source functions are extracted and used to solve for the overlaying acoustic field using a second independent model. In this manner, the acoustic field and flow field are one-way coupled: while the flow field creates and modifies the acoustic, the acoustic field cannot change the flow. Such a seperation is valid only in flow regions without significant non-linearity[30]. For low Mach number flows, which includes most hydroacoustic problems, the only regions with significant non-linearity would be those dominated by turbulence. In the present study, this would include the ships wake and boundary layer.

Two stage modeling offers a number of advantages. Since the fields are solved separately, appropriate grids and models can be chosen for each independently of the other, thus resolving the problem presented by scale differences. Feasibility studies have shown that both large eddy simulation and detached eddy simulation turbulence models should be adequate for hydro-acoustic study[3] [12] [33]. Two stage modeling allows the acoustic model to be re-run for differing acoustic conditions while retaining the basic flow information; since CFD modeling is by far more computationally expensive, this restarting option represents a considerable time savings. The disadvantage of such a process is that it is not general, and cannot be easily applied in flows where it is difficult to define linear and non-linear regions.

Once the problem has been seperated, a number of different approaches can then

be taken to solve for the acoustic field, with factors such as transmission distance, frequency bandwidth, and depth all playing a part. The simplest method conceptually is to discretize the wave equation over the area of interest. To avoid aliasing and other errors, the grid must be small enough to sample the highest frequency with two to eight points per wavelength, and should be uniform[20]. This method quickly becomes computationally expensive as higher frequencies and longer ranges are required. It is also difficult to define appropriate boundary conditions such that there are no false reflections from the far field[15][10]. More complicated methods of discretization exist to help address these issues, however they often require specific environmental conditions or more accurate knowledge of the boundary conditions than is available. For simulating ships in the open ocean, with the ranges of interest on the scale of kilometers, and large frequency bands, direct discretization is a poor choice.

Most noise models instead use one of several integral solutions to the wave equation. The first and most famous of these is Lighthill's acoustic analogy [18]. Lighthill was able to derive a form of the wave equation from a combination of the continuity and momentum conservation equations for fluid flow such that the source terms in his equation formed a stress tensor that could be obtained directly from turbulent flow information. With this equation he was able to show that the sound generated by this turbulent stress in a fluid flow was analogous to the sound in a stationary fluid with a proportional field of acoustic sources.

Curle extended Lighthill's solution in [9] to include the presence of solid boundaries. He was able to show that solid boundaries will result in an additional surface distribution of dipoles representing the force per area exerted on the fluid by the boundaries. Furthermore, he was able to show through dimensional analysis that this surface distribution will, in the limit of low Mach number, dominate the volume distribution in terms of the intensity of sound generated. In this way, the non-linearity caused by turbulence in the boundary layer can be safely neglected, and the acoustic problem can be solved directly at the ships hull.

Subsequently, Ffowcs Williams and Hawking were able to generalize Lighthill and Curle's work for objects in arbitrary motion[32]. Their equations have since become the standard on which most aeroacoustic noise models are now constructed. However, for simple low constant speed problems, such as the motion of a ship in the ocean,

the generalization to Ffowcs Williams-Hawking's equations is not needed, and in fact if incompressible flow is assumed they will reduce to Curle's equations. For application to the generation of noise by CFAV Quest, solving the Lighthill-Curle acoustic analogy in conjunction with the incompressible Navier-Stokes equations and an LES turbulence model will adequately capture the generation of hydrodynamic hull noise, with negligible error compared to the direct solution for the acoustic motions from the compressible Navier-Stokes equations[23].

Lighthill's and Curle's equations are exact in their solution for the noise in that they contain all the relevant effects of the generation and propagation of noise from flow in the free field. This includes effects such as the complicated reflection, diffraction and interference caused by the solid boundaries, and dispersion of acoustic energy through spherical spreading. It is important to note however that while these models can accurately model the source characteristics, they have been solved on a homogeneous infinite medium. The real ocean is obviously neither homogeneous nor infinite. As a result, neither of Lighthill's nor Curle's equations is capable of predicting the noise produced when there are interactions with sea boundaries, such as the surface or ocean floor, or effects due to inhomogeneity of the ocean, such as variable sound speeds or absorption spectra. In this manner, the Ligthill-Curle acoustic analogy is an exact solution for the problem of sound generation by flow in the free field, while the problem at hand requires the solution for sound generation by flow in a bounded field. It is therefore important to consider not only the generation of noise by fluid flow but also its propagation through space and time.

Recent work in the field has focused on the development of generalized acoustic analogies that can be adapted to suit the circumstances and propagation effects of interest. This work supposes that any acoustic analogy can be viewed as a wave operator applied to a flow solution, which is equal to a source function whose dependent variable is also the flow solution[11]. The difficulties then are whether or not the operator can be accurately inverted, and whether or not the source function accurately represents the propagation physics of interest. Lighthill's, Curle's and Ffowcs Williams-Hawking's equations can all be viewed in this manner, and work by Lilley[19], Goldstein[13], and others have demonstrated techniques for more general problems. The choice of acoustic analogy is now typically problem specific, and

different propagation physics can be included in either the source function or the propagation operator. Work on these methods is ongoing, and current results have shown that this approach can be very susceptible to errors from the CFD stage[30]. Additionally, nearly all of the research on such models has been done from the point of view of aeroacoustics. Propagation physics in the ocean is very different from propagation physics in the atmosphere, with phenomenon such as sea surface and floor interaction, and significant non-homogeneity of the fluid medium. Furthermore, such a method could not be generally applicable, as the propagation physics is tied to the source function. It is unclear whether the present techniques could be adapted to solve such problems, and so a different approach is needed.

The alternative is the inclusion of a third stage of modeling, which will simulate the effect of different propagation phenomena. Ocean acoustic propagation is well studied by oceanographers, and a number of computational frameworks are available. The simplest again assume a homogeneous ocean and quantify the effect of a phenomenon, such as absorption, using simple equations that can be added to the predicted signal[10]. However, work by Pederson [26] has shown that the homogeneous assumption can lead to drastic losses of accuracy in the far field for near surface simulations. In order to quantify the effect of a inhomogeneous ocean, more complex models are required.

The most widely used are ray theory models, wherein the sound wave fronts emitted from a source are discretized into a set of rays that travel outwards. The interaction of each ray with a boundary can then be modeled using simple equations for reflection and transmission. Inhomogeneity is included by discretizing the water column vertically, and including a refraction effect every time a ray moves between vertical layers. The resulting sound intensity at an observer can be determined from the number of arriving rays. Ray models suffer from a number of drawbacks however. They are prone to over predict shadow zones, or areas where sound will not arrive, and have difficulty resolving caustics, or areas where many rays will arrive[15]. Pederson has shown that these problems are particularly pronounced in longer ranges ($> 5km$) for near surface simulations[26], which are of particular importance for the present study. Ray models are also frequency limited, and give increasingly poor results as the spectrum of interest is lowered[10]. While ray models are limited by their

low frequencies, two step CFD and source models are limited in their high frequency resolution, as higher frequencies require increasingly small and computationally expensive time steps. Due to these conflicting restraints, ray theory is a poor choice for application with ship noise models.

Normal mode models are a prominent alternative modeling scheme. In normal mode models, the frequency response of the water column to excitation from acoustic sources is calculated for the spectrum of interest. This response takes the form of a number of modes of excitation. The horizontal propagation of these modes to an observer position can then be calculated, assuming no changes in the water column response. Accurate description of the boundaries of the water column, namely the sea surface and ocean floor, enable these models to accurately capture all effects of the bounded ocean. This model again uses a vertically discretized water column to account for changes in ambient conditions. While the interaction of the modes is less intuitive, the resulting model will be able to accurately reproduce the effects of reflection, refraction and transmission in the propagation. Pederson et al [27] have shown that normal mode models are capable of accurately predicting acoustic propagation in surface ducts to far greater ranges than ray theory models, and are not prone to over predict shadow zones and caustics. They are, additionally, not lower frequency limited.

Additional propagation models have been developed for a variety of other circumstances. Parabolic models assume that acoustic energy will propagate close to a reference speed in the fluid – either the shear or compressional speed depending on the problem. This assumption allows the elliptical wave equation to be recast as a parabolic equation, which can be solved easily from an initial solution using marching schemes. Marching schemes greatly simplifies the computation, provided the initial solution is known. Wave number integration or fast field techniques have a similar theoretical basis to normal mode models, but use different, and slightly more complex, mathematical techniques to solve them. These alternative techniques are more restrictive in their assumptions, and do not allow as wide a range of environmental conditions[10] [15]. They also require a more intimate knowledge of initial conditions than can generally be assumed, making them poor choices for the hydrodynamic noise problem.

1.2 Problem Statement

Previous work at Dalhousie University by Stefan Murphy, Dr. Julio Militzer and Dr. Mae Seto has developed a two step hydro-acoustic model with the goal of predicting the contribution of hydrodynamic hull noise to the acoustic signature of CFAV Quest, a DRDC (Defense Research and Development Canada) research ship [23]. This model combined Dr. Militzer's implementation of the Numerical Wind Tunnel (NWT) CFD package with an acoustic post processor developed by Murphy that was based on a modified version of Curle's solution to Lighthill's equation.

The NWT is a powerful CFD package developed over many years by Dr. Militzer and his colleagues, and contains a number of features useful for the combination with an acoustic post processor. In the CFD step, the Navier-Stokes equations are discretized using a finite volume method over an unstructured Cartesian grid. This mesh is anisotropic adaptive, and is combined with an immersed boundary method for the specification of boundary conditions. These features greatly aid problem setup by reducing the time required for grid generation. It also uses a 3D unsteady implicit discretization of the equations, with Crank-Nicholson time advancement at a constant time step, which is a highly accurate method for unsteady flow. Additionally, it has parallelization and automatic load rebalancing for distributed processing, which greatly speeds up computation[6]. Finally, it features a hybrid LES turbulence model developed specifically for use in acoustic applications[23].

Murphy went on to validate this combination of the NWT package with his acoustic post processor against a benchmark problem of flow around a circular cylinder. The final results of his simulations were shown to over-predict the sound pressure levels found in an at-sea trial of the Quest[23]. It was hypothesized that this over-prediction was due to interactions with the sea surface, which were not included in the post processor. The aim of the current work is to develop a propagation model to accurately capture those effects. To this end, three propagations models have been developed for comparison. Two of these models, a simple source model and a normal mode model, have been adapted from literature; the third, a method of images solution to the Lighthill-Curle equations, is of the authors design. The accuracy of the CFD simulations will also be investigated using newly-available experimental data for the ship's hull pressure fluctuations. The following sections are laid out such that

chapter 2 will present the theory of sea surface effects and the derivation of the implemented models, chapter 3 will present and compare the results of the CFD simulation and the experimental hull pressure fluctuations, chapter 4 will present and compare the results of the propagation models with experimental sound measurements, and chapter 5 will present conclusions and recommendations for future work.

Chapter 2

Theory of Acoustic Modeling

Any process that creates an unsteady pressure field in a fluid medium can result in sound. The hybrid methodology simplifies the hydrodynamic sound problem by separating the generation and propagation of that sound from the physical flow that creates it. As this study focuses on the modeling of the generation and propagation of that sound, and the impact of a free sea surface, it will not present details on the methodology of computational fluid dynamics. For a detailed discussion of the Numerical Wind Tunnel CFD package and its use in conjunction with the acoustic post-processor, please see [23] or [6].

This chapter first focuses on the generation of acoustic energy. It begins with a discussion of acoustic sources, their efficiencies, and how to describe them mathematically. It will then go on to derive the Lighthill and Curle equations, and present details of their implementation in the post processor. Following the discussion on the generation of acoustic energy, the focus will shift to its propagation. The Lloyd's Mirror effect of the sea surface will be introduced, including a discussion of two propagation modeling methods. This discussion will be followed with details on the effect of a variable speed of sound on acoustic propagation, and the presentation of the Normal Mode model to account for it. The method of images model, and the results from all three propagation models, are the fundamental results of this study.

2.1 Source Modeling

In the hybrid methodology implemented in this study, the generation of sound from flow has been split from the flow itself, as well as from the propagation of that sound into the far field. This section will focus on the theoretical background of the sound generation stage.

2.1.1 Acoustic Sources

Noise sources in a fluid can be classified by the physical mechanism that they use to convert non-radiating flow energy into radiating acoustic energy. These classifications each correspond mathematically to the dominant order of a multipole source. The order of the pole will describe the directionality of the source, as well as the efficiency of the flow-to-acoustic energy conversion. Only the first three such poles play a significant role in subsonic flow acoustics[29].

Monopoles

Monopoles are zero order multipoles and physically correspond to fluctuations in volume, mass, or heat. They can be represented as a pulsating sphere, and are omnidirectional and spherically symmetrical. Monopoles can. however. have directional character when they are assembled into arrays, due to interference. Monopoles can only be present at fluid boundaries, due to the physical mechanisms that create them. Figure 2.1 shows a simple 2D representation of a monopole and its radiation pattern.

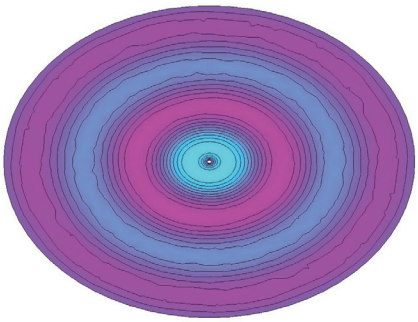

Figure 2.1: Monopole radiation pattern

The efficiency of an acoustic source is calculated from the radiation efficiency, defined as the ratio of acoustic power to the total power of the acoustic and flow fields. Expressed in terms of characteristic frequency ω, reference length l_0, flow speed u_0 and Mach number M, the radiation efficiency of a monopole source is:

$$\eta_{rad} = \left(\frac{\omega l_0}{u_0}\right) M \tag{2.1}$$

Examples of monopole sources include pulsating bubbles, unsteady combustion processes, cavitation, and heat or mass injection. Fluid structure interaction can

result in unsteady flexing of hull plating, which is also a major source of monopole noise. Monopole sources on CFAV Quest include propeller cavitation, hull plate flexion, fluid injection by bow thrusters, fluid flow over thruster apertures, and the presence of air bubbles in the fluid along the hull. However, this study does not include the effects of either the propeller or fluid structure interaction, the CAD model in use removes the bow thrusters for simplicity, and the effects of air bubbles are not considered. As such, monopole sources of sound will not be considered.

Dipoles

Dipoles are first order multipoles, and correspond to fluctuating forces. A solid boundary is again required, in order to introduce the fluctuating forces that convert into sound pressure. Dipoles are represented mathematically as two equal monopoles of opposite phase, located a small (relative to their wavelength) distance apart. The fluid between them is subject to a fluctuating force due to their changing phases, resulting in radiation of acoustic energy in a cosine directional pattern, as shown in figure 2.2. The radiation efficiency of a dipole source is given as

$$\eta_{rad} = \frac{1}{2}\left(\frac{\omega l_0}{u_0}\right)^3 M^3 \tag{2.2}$$

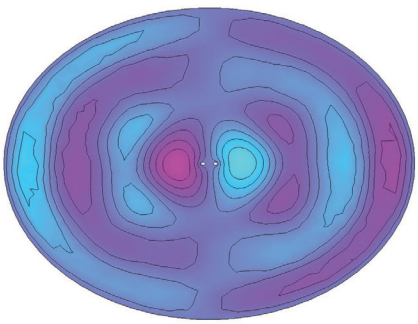

Figure 2.2: Dipole radiation pattern

Dipole sources are extremely common in most fluid noise applications, and can include phenomenon like rotor blades, control surfaces, and vortex shedding. A major source of dipole noise in ships is the propeller. However, the propeller has a very well defined frequency range, and is so dominant that it is easily detected and distinguished

in measurements. The noise produced by unsteady fluid flow over a solid surface is a dipole source, and is the dominant sound source in the hydrodynamic hull noise problem.

Quadropoles

Finally, quadropoles are multipoles of second order and have as their physical basis fluctuating stress. Fluctuating stresses are the result of turbulent motion within the fluid itself, and therefore can be caused independently of any solid boundaries. They can be represented as either four monopoles of alternating phase or two dipoles of opposite phase, and can be arranged either in a line or as a square (shown in figure 2.3). The result has no net fluctuation of fluid or forces, but does have fluctuating Reynolds stress due to turbulence, which results in the generation of sound waves. The efficiency of quadropole sources is given by:

$$\eta_{rad} = \frac{1}{27}\left(\frac{\omega l_0}{u_0}\right)^5 M^5 \tag{2.3}$$

The turbulent fluid that surrounds any object, or even in the absence of an object, is itself a source of quadropole noise. However, as can be seen from equation 2.3, the efficiency is proportional to the fifth power of the Mach number. Therefore for most subsonic applications with $M << 1$ the generation of quadropole noise is so inefficient as to be negligible.

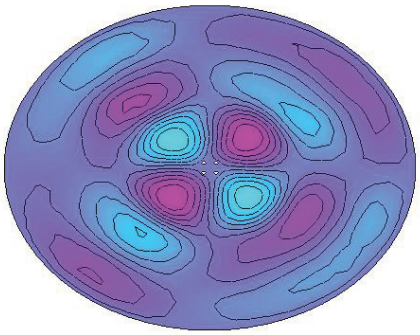

Figure 2.3: Quadropole radiation pattern

2.1.2 Lighthill's Equation

The problem of predicting noise generated strictly from fluid flow was first tackled by M.J. Lighthill in 1951[18]. Lighthill postulated that the sound generated by fluid flow was caused by turbulent fluctuations within the flow, in the form of a stress tensor. The fluctuating stress tensor was then used as a forcing function on a uniform free field at rest. His equation showed that a distribution of quadropole sources on a uniform resting field, whose strength was proportional to the fluctuating stress tensor, would produce hydrodynamic noise analogous to that produced by the flow. What follows is a brief version of Lighthills derivation of the acoustic analogy.

Beginning with the governing equations of fluid flow with no external forces, the continuity equation is expressed as:

$$\frac{\partial \rho}{\partial t} + \frac{\partial}{\partial x_i}(\rho u_i) = 0, \tag{2.4}$$

and the Reynolds form of the momentum equation as:

$$\frac{\partial}{\partial t}(\rho u_i) + \frac{\partial}{\partial x_i}(\rho u_i u_j + p_{ij}) = 0, \tag{2.5}$$

where ρ is density, u_i is velocity, and p_{ij} is pressure. By the elimination of the momentum density (ρu_i) from each, Lighthill arrives at an inhomogeneous wave equation of the form

$$\frac{\partial^2 \rho}{\partial t^2} - a_0^2 \nabla^2 \rho = \frac{\partial^2}{\partial x_i \partial x_j}(T_{ij}), \tag{2.6}$$

where a_0 is the ambient speed of sound. The source term contains the stress tensor

$$T_{ij} = \rho u_i u_j + p_{ij} - a_0^2 \rho \delta_{ij}, \tag{2.7}$$

which is known as Lighthills stress tensor. The general solution of 2.6 is given by

$$\rho - \rho_0 = \frac{1}{4\pi a_0^2} \int_V \frac{\partial^2 T_{ij}}{\partial y_i \partial y_j} \frac{d\mathbf{y}}{|\mathbf{x} - \mathbf{y}|} + \frac{1}{4\pi} \int_S \left(\frac{1}{r} \frac{\partial \rho}{\partial n} + \frac{1}{r^2} \frac{\partial r}{\partial n} \rho + \frac{1}{a_0 r} \frac{\partial r}{\partial n} \frac{\partial \rho}{\partial t} \right) dS(\mathbf{y}), \tag{2.8}$$

where $r = |\mathbf{x} - \mathbf{y}|$, n is the normal vector pointing outward from the fluid, and the quantities $\frac{\partial^2 T_{ij}}{\partial y_i \partial y_j}$,$\frac{\partial \rho}{\partial n}$,$\rho$,$\frac{\partial \rho}{\partial t}$ are taken at the retarded time $t - r/a_0$. Here, the integration volume V is taken to be external to any solid boundaries such as a ship hull, and the integration surface S is taken over the surface of such a solid boundary.

In his original derivation, Lighthill was interested in the solution for flows without the presence of solid boundaries, and so the surface integral was taken to be 0 and the solution reduced to the retarded potential,

$$\rho - \rho_0 = \frac{1}{4\pi a_0^2} \int_V \frac{\partial^2 T_{ij}}{\partial y_i \partial y_j} \frac{d\mathbf{y}}{|\mathbf{x}-\mathbf{y}|}. \tag{2.9}$$

It can be seen that the sound radiates as if from a distribution of quadropole sources whose strength is given by T_{ij}. Lighthill went on to simplify this solution by imagining a quadropole field as the limit of four separate single source fields coming infinitely closer together. Equation 2.9 then simplifies down to

$$\rho - \rho_0 = \frac{1}{4\pi a_0^2} \frac{\partial^2}{\partial x_i \partial x_j} \int_V \frac{T_{ij}(\mathbf{y}, t - \frac{|\mathbf{x}-\mathbf{y}|}{a_0})}{|\mathbf{x}-\mathbf{y}|} d\mathbf{y}. \tag{2.10}$$

2.1.3 Curle's Equation

Curle went on to expand upon Lighthill's analogy by including the effects of solid boundaries on the flow, such as from the walls of the ship. Solid boundaries will influence the sound predicted by Lighthill's equation in two ways: first, the surface integral from 2.8 will not disappear, and second, the volume integral will be modified to account for reflections of the quadropole noise off of the solid boundary. The surface integral is first simplified by

$$\begin{aligned}
&\int_S \left\{ \frac{1}{r}\frac{\partial \rho}{\partial n} + \frac{1}{r^2}\frac{\partial r}{\partial n}\rho + \frac{1}{a_0 r}\frac{\partial r}{\partial n}\frac{\partial \rho}{\partial t} \right\} dS(\mathbf{y}) \\
&= \int_S l_i \left\{ \frac{1}{r}\frac{\partial \rho}{\partial y_i} + \frac{1}{r^2}\frac{\partial r}{\partial y_i}\rho + \frac{1}{a_0 r}\frac{\partial r}{\partial y_i}\frac{\partial \rho}{\partial t} \right\} dS(\mathbf{y}) \\
&= \int_S l_i \frac{1}{r}\frac{\partial}{\partial y_i}(\rho \delta_{ij}) dS(\mathbf{y}) - \int_S l_i \left\{ \frac{1}{r^2}\frac{\partial r}{\partial x_i}\rho + \frac{1}{a_0 r}\frac{\partial r}{\partial x_i}\frac{\partial \rho}{\partial t} \right\} dS(\mathbf{y}) \\
&= \int_S l_i \frac{1}{r}\frac{\partial}{\partial y_i}(\rho \delta_{ij}) dS(\mathbf{y}) + \int_S l_i \frac{\partial}{\partial x_i}(\frac{1}{r}\rho \delta_{ij}) dS(\mathbf{y}),
\end{aligned} \tag{2.11}$$

where l_i are the direction cosines of the outward normal from the fluid ($(l_1, l_2, l_3) = \mathbf{n}$), and the retarded time identity

$$\frac{\partial}{\partial x_i}\left\{ \frac{1}{r} f(t - \frac{r}{a_0}) \right\} = -\left\{ \frac{1}{r^2} f + \frac{1}{a_0 r} f' \right\} \frac{\partial r}{\partial x_i},$$

was used on the second surface integral.

In equation 2.10 Lighthill simplified the volume integral by assuming the quadropole sources to be the limiting case of a distribution of point sources coming infinitely close

together. This assumption is not valid in the presence of solid surfaces, and so an alternative is required. Curle realized that this assumption is analogous to twice applying the divergence theorem to the volume integral, yielding first

$$\begin{aligned}\int_V \frac{\partial^2 T_{ij}}{\partial y_i \partial y_j}\frac{d\mathbf{y}}{r} - \frac{\partial}{\partial x_i}\int_V \frac{\partial T_{ij}}{\partial y_j}\frac{d\mathbf{y}}{r} &= \int_V \frac{\partial}{\partial y_i}\left[\frac{\partial T_{ij}}{\partial y_j}/r\right] d\mathbf{y} \\ &= \int_S l_i \frac{\partial T_{ij}}{\partial y_j}\frac{dS(\mathbf{y})}{r}, \end{aligned} \tag{2.12}$$

and second

$$\int_V \frac{\partial T_{ij}}{\partial y_j}\frac{d\mathbf{y}}{r} - \frac{\partial}{\partial x_j}\int_V T_{ij}\frac{d\mathbf{y}}{r} = \int_S l_j T_{ij}\frac{dS(\mathbf{y})}{r}. \tag{2.13}$$

Combing 2.12 and 2.13 gives

$$\begin{aligned}\int_V \frac{\partial^2 T_{ij}}{\partial y_i \partial y_j}\frac{d\mathbf{y}}{r} &= \frac{\partial^2}{\partial x_i \partial x_j}\int_V \frac{T_{ij}(\mathbf{y}, t-\frac{r}{a_0})}{r} d\mathbf{y} \\ &+ \frac{\partial}{\partial x_i}\int_S l_j T_{ij}\left(\mathbf{y}, t-\frac{r}{a_0}\right)\frac{dS(\mathbf{y})}{r} + \int_S l_i \frac{\partial T_{ij}}{\partial y_j}\frac{dS(\mathbf{y})}{r}, \end{aligned} \tag{2.14}$$

and substituting both 2.14 and 2.11 into 2.8 will then result in

$$\begin{aligned}\rho - \rho_0 &= \frac{1}{4\pi a_o^2}\frac{\partial^2}{\partial x_i \partial x_j}\int_V \frac{T_{ij}(\mathbf{y}, t-\frac{r}{a_0})}{r} d\mathbf{y} \\ &+ \frac{1}{4\pi a_0^2}\int_S l_i \frac{1}{r}\frac{\partial}{\partial y_j}(T_{ij} + a_0^2 \rho \delta_{ij}) dS(\mathbf{y}) \\ &+ \frac{1}{4\pi a_0^2}\frac{\partial}{\partial x_i}\int_S l_j \frac{1}{r}(T_{ij} + a_0^2 \rho \delta_{ij}) dS(\mathbf{y}). \end{aligned} \tag{2.15}$$

By substituting in Lighthill's stress tensor, 2.7, equation 2.15 becomes

$$\begin{aligned}\rho - \rho_0 &= \frac{1}{4\pi a_0^2}\frac{\partial^2}{\partial x_i \partial x_j}\int_V \frac{T_{ij}(\mathbf{y}, t-\frac{r}{a_0})}{r} d\mathbf{y} \\ &+ \frac{1}{4\pi a_0^2}\int_S l_i \frac{1}{r}\frac{\partial}{\partial y_j}(\rho v_i v_j + p_{ij}) dS(\mathbf{y}) \\ &+ \frac{1}{4\pi a_0^2}\frac{\partial}{\partial x_i}\int_S l_j \frac{1}{r}(\rho v_i v_j + p_{ij}) dS(\mathbf{y}). \end{aligned} \tag{2.16}$$

Since $l_i \frac{\partial}{\partial y_j}(\rho u_i u_j + p_{ij}) = -l_i \frac{\partial}{\partial t}(\rho u_i)$, and given that it is required that any surface is fixed or vibrating on its own plane, then $l_i u_i \equiv 0$ and 2.16 reduces to

$$\rho - \rho_0 = \frac{1}{4\pi a_0^2}\frac{\partial^2}{\partial x_i x_j}\int_V \frac{T_{ij}(\mathbf{y}, t-\frac{r}{a_0})}{r} d\mathbf{y} - \frac{1}{4\pi a_0^2}\frac{\partial}{\partial x_i}\int_S \frac{P_i(\mathbf{y}, t-\frac{r}{a_0})}{r} dS(\mathbf{y}), \tag{2.17}$$

where $P_i = -l_i p_{ij}$. Equation 2.17 is Curle's solution for the sound generated aerodynamically in the presence of solid boundaries, and shows that the sound field can be

thought of as a volume distribution of quadropoles whose strength is proportional to the turbulent stress, and a surface distribution of dipoles whose strength is proportional to the pressure force exerted on the fluid by the boundaries. Curle was then able to show through a dimensional analysis that quadropole sources will have a negligible influence on the sound field as compared to the dipoles, due to the difference in their efficiency as sources.

The acoustic post processor uses a modified version of Curle's solution, wherein the spatial derivatives have been transformed into temporal ones, and the equations rearranged so that the derivatives are located within the integrals instead of without. These modifications were made to simplify the coding and implementation procedures. Details on the derivation of the modified version can be found in Larsson et al[17], while the implementation and discretization can be found in [23].

2.2 Propagation Modeling

Two step hydroacoustic models are excellent tools for modeling the generation of sound from the turbulent motions of fluid, but they are often inadequate for predicting the observable noise at an arbitrary location. Once generated, acoustic waves must travel or propagate through an often complex medium before arriving at an observer, potentially a considerable distance from the sound source. To arrive at an accurate result, the models used to generate flow noise must be coupled with accurate propagation models that can capture the relevant acoustic effects of the environment in which they travel.

The Lighthill and Curle solutions to the acoustic analogy problem both give excellent results for the generation of sound and its propagation in the near field close to the source. While they are exact solutions of the aerodynamic sound problem as posed by Lighthill and Curle, their description of that problem involved a homogeneous infinite medium, which is not the case here. In an infinite, homogeneous medium, the propagation of an acoustic signal is relatively straightforward. A point source would radiate sound equally in all directions, and the signal strength would drop proportionally with distance. This drop is because while the acoustic energy emitted by the source is constant, the area that that energy travels through is constantly increasing. The intensity of the sound heard is defined as the sounds power

per unit area, $I = \frac{p^2}{\rho a_0}$, and is analogous to the flux of acoustic energy through a point. As the sound propagates through the ocean as a spherical wave, the surface area of the sphere will increase with distance. While the flux remains constant the intensity will therefore drop proportionally; this phenomenon is referred to as spherical spreading. Spherical spreading, and all other propagation effects, is typically measured in terms of a transmission loss, or the ratio of a reference intensity to the intensity at the observer. The transmission loss due to spherical spreading is given by equation 2.18:

$$TL = -20 \log r. \tag{2.18}$$

The acoustic post processor, as built from Curle's solution, is more than capable of handling the effects of spherical spreading, however the assumption of an infinite homogeneous medium can cause significant problems when applied to a real medium such as the ocean. The ocean is not infinite, and the presence of the sea surface and floor can cause significant propagation effects. Nor is it homogeneous. The properties of the ocean can change continuously with both depth and range due to distributions of salinity and temperature, and also discontinuously due to the presence of other structures or marine life. Effects of inhomogeneity include absorption, wherein different frequencies of sound are dissipated due to the action of viscosity or density variation, and refraction due to variations in the local sound speed. This study focuses generally on the effect of the sea surface, and specifically on the Lloyd's Mirror effect it creates. It will also include a discussion on variation due to sound speed gradients, but does not explore other phenomenon such as absorption.

2.2.1 Lloyd's Mirror Interference

The presence of a bounding half plane in an acoustic medium, such as the sea surface, significantly alters acoustic propagation. In an unbounded flow the only path a signal can take from a source to a receiver is the straight line or direct path (DP) between the two. Sound, however, can reflect off of the ocean surface, which creates a second surface reflected path (SRP) that the sound can and will travel along to arrive at the source. These two propagation paths are illustrated in figure 2.4.

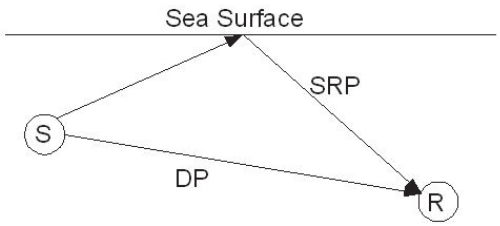

Figure 2.4: Propagation paths in the Lloyd's Mirror effect

When a wave hits a boundary and is reflected, it is not unaltered. The act of reflection will cause the wave to undergo a 180° phase shift, and will also modulate the amplitude according to how rough the ocean surface is. This effect varies from a simple loss of amplitude in the case of rough seas, to the superimposition of some portion of the sea states frequency content onto the signal, in the case of dominant swell. For the purposes of this discussion, the sea state is taken to be calm and the ocean surface is assumed to be acoustically smooth, meaning amplitude modulation is negligible.

When the two signals recombine at the receiver, they will superimpose on each other and cause interference. The surface reflected path will not only have a 180° phase shift due to the reflection, but will also have a second phase shift that is due to differences in travel time along the two paths. When they recombine, they will produce a unique interference pattern that is referred to as the Lloyds Mirror Effect. Figure 2.5 shows a typical Lloyds Mirror interference pattern. This type of propagation effect can have a significant impact on acoustic propagation, and is the major effect of the ocean surface.

In general, the pattern can be divided into three distinct regions based on the range. In the near field region, typically within 250 m of the source, the surface reflected path will be much longer than the direct path, resulting in a much higher attenuation from distance. When they recombine, the surface reflected path will not have the strength to cause significant interference, and the effect is generally negligible within this region. In the intermediate field from approximately 250 m to 5 km, the travel time between the signals begins to be comparable. The peaks and nulls in the interference are created by the phase difference between the signals cycling between in-phase and out-of-phase conditions. Peaks correspond to a nearly in-phase state

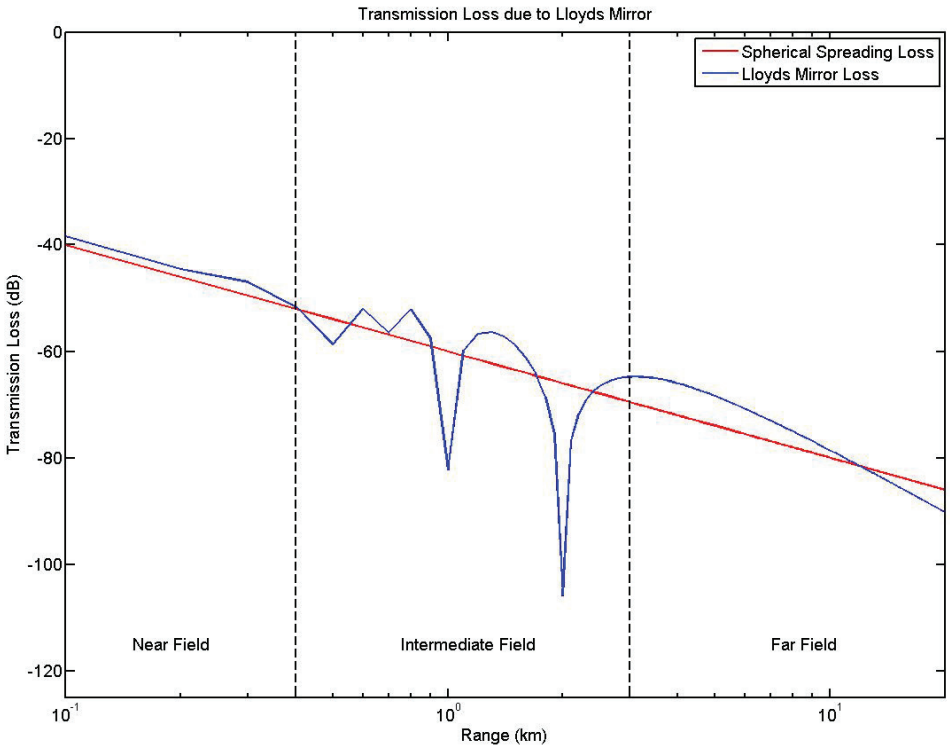

Figure 2.5: Example Lloyd's Mirror interference pattern. Source depth 50m, receiver depth 100m, frequency 300 Hz

where the signal is practically doubled, while nulls correspond to the out-of-phase state where the signal is nearly eliminated. Finally, in the far field region, the signals are increasingly out of phase as the two paths become identical, resulting in a steadily increasing transmission loss. The far field loss can be approximated as twice that of spherical spreading, or $-40 \log r$.

A general expression for the Lloyd's Mirror transmission loss can be difficult to obtain for all but the simplest of sources. For a point source transmitting at a single frequency, the acoustic pressure field can be determined from

$$p(r, z) = \frac{e^{ikR_1}}{R_1} - \frac{e^{ikR_2}}{R_2}, \tag{2.19}$$

with $R_1 = \sqrt{r^2 + (z - z_s)^2}$ and $R_2 = \sqrt{r^2 + (z + z_s)^2}$. Here, r is the horizontal range between source and observer, z is the observer depth, z_s is the source depth, and k is the wave number of the source. Remembering that the transmission loss is just the

ratio of the intensities, the Lloyd's mirror transmission loss can then be calculated with regards to a reference pressure p_0 by

$$TL = 20 \log \frac{|p(r,z)|}{|p_0|}. \tag{2.20}$$

Combined, equations 2.19 and 2.20 represent the solution for the Lloyd's Mirror interference of a simple source vibrating at a single frequency, and can be applied to the entire spectrum of interest. These equations are presented here in the form taken from [15], however they are well known and appear in several different forms throughout the literature. It is the first of three propagation models investigated in this study, and will be referred to as the simple source model.

2.2.2 Method of Images

As stated in the previous section, equation 2.19 assumes a simple point source vibration at a single frequency, close to the sea surface. A simple point source is assumed to be acoustically compact; that is, it is small when compared to the wavelength of sound it produces. For a complex shape such as a ship, which will emit a sound over a broadband instead of a single frequency, it is not reasonable to make this compactness assumption. While equation 2.19 can still be used to generate reasonable approximations of the Lloyd's Mirror transmission loss, a more physically accurate model would be preferable.

The derivation of equation 2.19 begins with a point source located near an acoustic half plane, as was shown in figure 2.4. Rather than model the SRP path and its reflection from the surface, the medium is modeled as infinite, and the source is mirrored about the surface to create a second "image" source. This image source is taken to be 180° out of phase with the real source. In this way, the straight line image path in figure 2.6, can be taken as analogous to the surface reflected path in figure 2.4

The principle of superposition states that in a linear system, the total response of a system to multiple inputs can be obtained from the superposition of the responses to the individualized inputs. Using this principle to combine the sounds from the direct path and image path of a simple acoustic source results in equation 2.19. From the same principle, a Lloyd's Mirror model for a complex, acoustically non-compact source

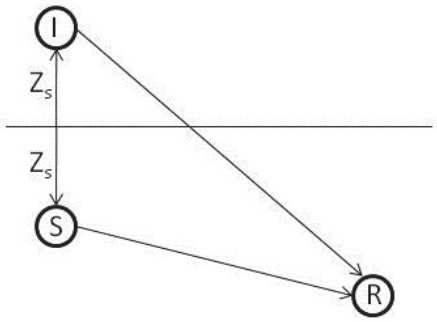

Figure 2.6: Image and real source direct paths

can be obtained by creating an image of the ship, mirrored about the sea surface and 180° out of phase. The Lighthill-Curle equations can then be re-solved for this image ship, and the two solutions superimposed at the receiver position. This methodology comprises the second propagation model, called the method of images. To the authors knowledge, a method of images solution to the Lighthill-Curle acoustic analogy for the problem of hydrodynamic generation of sound in the vicinity of a reflecting half plane has not been previously attempted, and so represents a significant new contribution to the field of hydroacoustics.

2.2.3 Normal Mode Models

The second restricting assumption of the Lighthill-Curle equations was the homogeneity of the medium. The ocean is a complex medium and is often inhomogeneous, both radially and vertically. Radial changes are often caused by ocean currents, biological processes, and physical structures, and are therefore difficult to account for in a general model, and will not be considered. Vertical inhomogeneity can be more easily measured, modeled and predicted. Heating and cooling from the sun and sea surface will create gradients of temperature and salinity, which will ultimately result in a varying speed of sound through the vertical water column.

As sound moves through a medium with a varying speed of sound, it will undergo refraction. This refraction will cause the path followed by a sound signal to curve, resulting in drastically more complex Lloyd's Mirror geometry. Studies by Pederson [26] have shown that the assumption of a constant speed of sound in cases involving

Lloyd's Mirror can lead to a loss of far-field accuracy as high as 40 dB.

Normal mode models are one set of models developed by physical oceanographers for dealing with varying sound speed gradients. What follows is the derivation of a normal mode model as presented in [15]. The ocean is taken to be radially symmetrical, giving the wave equation for acoustic pressure,

$$\nabla^2 p(r,z) - \frac{1}{c(z)^2}\frac{\partial^2 p(r,z)}{\partial t^2} = 0, \tag{2.21}$$

where $c(z)$ is the local speed of sound. The wave equation is then transformed via the Fourier transform into the Helmholtz equation,

$$\frac{1}{r}\frac{\partial}{\partial r}\left(r\frac{\partial p(r,z)}{\partial r}\right) + \rho(z)\frac{\partial}{\partial z}\left(\frac{1}{\rho(z)}\frac{\partial p(r,z)}{\partial z}\right) + \frac{\omega^2}{c^2(z)}p(r,z) = -\frac{\delta(r)\delta(z-z_s)}{2\pi r}. \tag{2.22}$$

It is assumed that there is a solution to the unforced equation of the form $p(r,z) = \Phi(r)\Psi(z)$. This solution is substituted into equation 2.22; dividing through by $\Phi(r)\Psi(z)$ results in

$$\frac{1}{\Phi(r)}\left[\frac{1}{r}\frac{d}{dr}\left(r\frac{d\Phi(r)}{dr}\right)\right] + \frac{1}{\Psi(z)}\left[\rho(z)\frac{d}{dz}\left(\frac{1}{\rho(z)}\frac{d\Psi(z)}{dz}\right) + \frac{\omega^2}{c^2(z)}\Psi(z)\right] = 0. \tag{2.23}$$

Since the terms inside the square brackets are functions of only r and z, respectively, this equation is solvable by the method of separation of variables. Setting the terms equal to the separation constant ξ^2 yields the modal equation,

$$\rho(z)\frac{d}{dz}\left[\frac{1}{\rho(z)}\frac{d\Psi(z)}{dz}\right] + \left[\frac{\omega^2}{c^2(z)} - \xi^2\right]\Psi(z) = 0, \tag{2.24}$$

and the range equation,

$$\frac{d}{dr}\left(r\frac{d\Phi(r)}{dr}\right) - r\Phi(r)\xi^2 = 0. \tag{2.25}$$

The modal equation, 2.24, is a regular Sturm-Liouville problem. Its boundary conditions are taken to be the pressure release condition at the surface, $\Psi(0) = 0$, and a perfectly rigid sea floor, $\frac{d\Psi}{dz}|_{z=D} = 0$, where D is the channel depth. The equation will have an infinite number of solutions $\Psi_m(z)$ which are analogous to the modes of vibration for a string of length D. Each solution is unique and is paired with a horizontal propagation constant ξ^2. The functions $\Psi_m(z)$ are referred to as the modes or eigenfunctions of the solution, and ξ^2 as the mode numbers or eigenvalues. The mth mode will have m zeroes on the interval $[0, D]$ and the mode numbers will

all be real and ordered such that $\xi_1^2 > \xi_2^2 > \xi_3^2$.... The mode scaling is arbitrary, but will be here normalized such that

$$\int_0^D \frac{\Psi_m^2(z)}{\rho(z)} dz = 1. \tag{2.26}$$

Additionally, the modes are orthogonal, requiring that

$$\int_0^D \frac{\Psi_m(z)\Psi_n(z)}{\rho(z)} dz = 0, \ m \neq n. \tag{2.27}$$

The final important property of the solution to the modal equation is that the modes form a complete set, and therefore we can represent the pressure as a sum of the normal modes,

$$p(r,z) = \sum_{m=1}^{\infty} \Phi_m(r)\Psi_m(z). \tag{2.28}$$

Using this relation, equation 2.22 can be rewritten as

$$\begin{aligned} &\sum_{m=1}^{\infty} \left\{ \frac{1}{r}\frac{d}{dr}\left(r\frac{d\Phi_m(r)}{dr} \right) \Psi_m(z) \right. \\ &\left. +\Phi_m(r)\left[\rho(z)\frac{d}{dz}\left(\frac{1}{\rho(z)}\frac{d\Psi_m(z)}{dz} \right) + \frac{\omega^2}{c^2(z)}\Psi_m(z) \right] \right\} = -\frac{\delta(r)\delta(z-z_s)}{2\pi r}, \end{aligned} \tag{2.29}$$

which can be simplified by use of the modal equation 2.24 to yield

$$\sum_{m=1}^{\infty} \left\{ \frac{1}{r}\frac{d}{dr}\left(r\frac{d\Phi_m(r)}{dr} \right) \Psi_m(z) + \xi_m^2 \Phi_m(r)\Psi_m(z) \right\} = -\frac{\delta(r)\delta(z-z_s)}{2\pi r}. \tag{2.30}$$

The operator $\int_0^D (\cdot)\frac{\Psi_n(z)}{\rho(z)}dz$ is then applied to equation 2.30, and due to the orthogonality property, 2.27, only the nth term will remain in the sum,

$$\frac{1}{r}\frac{d}{dr}\left[r\frac{d\Phi_n(r)}{dr} \right] + \xi_n^2\Phi_n(r) = -\frac{\delta(r)\Psi_n(z_s)}{2\pi r\rho(z_s)}. \tag{2.31}$$

The solution to equation 2.31 is given in terms of a Hankel function,

$$\Phi_n(r) = \frac{i}{4\rho(z_s)}\Psi_n(z_s)H_0^{(1)}(\xi_n r). \tag{2.32}$$

The solution for the acoustic pressure is therefore

$$p(r,z) = \frac{i}{4\rho(z_s)} \sum_{m=1}^{\infty} \Psi_m(z_s)\Psi_m(z)H_0^{(1)}(\xi_m r), \tag{2.33}$$

which is rewritten in terms of the asymptotic approximation

$$p(r,z) \simeq \frac{i}{\rho(z_s)\sqrt{8\pi r}} e^{-i\pi/4} \sum_{m=1}^{\infty} \Psi_m(z_s)\Psi_m(z) \frac{e^{i\xi_m r}}{sqrt\xi_m}. \tag{2.34}$$

Equation 2.34 can be expressed in terms of transmission loss, with the reference pressure taken to be $p_0(r) = \frac{e^{i\xi_0 r}}{4\pi r}$, as

$$TL(r,z) \simeq -20\log\left|\frac{1}{\rho(z_s)}\sqrt{\frac{2\pi}{r}}\sum_{m=1}^{\infty}\Psi_m(z_s)\Psi_m(z)\frac{e^{i\xi_m r}}{sqrt\xi_m}\right|. \tag{2.35}$$

Normal mode models can be viewed then as solving for the response of the vertical water column to the excitation from an acoustic source, in this study the ship CFAV Quest. This response is expressed in terms of a sum of modes, which are varyingly damped as they propagate into the far field. The interaction of these modes will combine to give the total response of the system at a given receiver point, and will include the effects of the water column boundary conditions, such as the Lloyd's Mirror effect. Critical factors for the development of a normal mode model include the number of modes utilized and their sampling, as well as the sound speed profile taken for the vertical water column. These parameters will be explored in more detail in section 4.2.2. A normal mode model as presented above is the final propagation model investigated.

2.2.4 Implementation

Three different methodologies for modeling the propagation of acoustic sound into the far field of the near surface ocean environment have been presented. They include the Lloyd's Mirror equation for an acoustically compact source, or simple source model, the method of images, and a normal mode propagation model. The implementation of these three models into the existing acoustic post-processor will be specific to the varying needs of each.

The method of images is unique among the propagation models in that it is solved in the time domain, and must be computed along with the solution to the standard Lighthill-Curle equation. It is therefore the first to be called in the post-processor, and the most seamlessly implemented. As discussed above, the post-processor simply assumes a second image ship in the infinite medium, mirrored about the sea surface from the real ship. The calculations for the Lighthill-Curle equations are then

repeated at every time step, calculating a second image signal in addition to the original signal. Once both time signals have been calculated, a phase correction must be added to the image signal. The Lighthill-Curle equations are calculated in terms of retarded time $t - r/a_0$, however the receiver time r will be a seperate time vector for both the real and image signals. If the image signal is not modified, there will be no phase difference between the image and real signal, and so no Lloyd's Mirror interference will arise. The discretized phase difference is calculated based on the difference in path length, and the image signal is then delayed by padding the front of the signal with mean values. The 180° phase shift is then applied to the image signal, and both signals are added to yield the superposition solution. Both the superposition signal and the real source signal are output by the post-processor, and the real source signal is passed to the two remaining propagation models. As the method of images solution is an original method, this implementation is also original and of the author's design.

The remaining models both express their solutions in terms of a transmission loss in the frequency domain. The signal output by the post-processor must therefore also be transformed into its power-spectral density in order to implement these models. A spectrogram of the signal is taken; time and frequency parameters are customizable so that desired fidelities for the time and frequency components can be achieved. The time-frequency domain of the spectrogram is then passed to the simplified source model, which solves for the expected transmission loss over the domain due to Lloyd's Mirror interference, as per equations 2.19 and 2.20. The difference between the predicted loss from Lloyd's Mirror and that predicted by spherical spreading is then calculated and added to the spectrogram, which is then taken as the output of the simplified source model. This implementation follows basic practice as presented in [10],[29], and [15].

The process for the normal mode calculations is similar but more complex. The time-frequency domain of the original signal's spectrogram is passed to the normal mode model. Equation 2.35 is solved on the domain, having been discretized as follows. As with the derivation, the discretization and implementation presented here follow that utilized by Jensen et al in [15].

The water column is discretized from z=0 to z=D into N equal intervals with mesh width $h = D/N$. The modal equation, 2.24, will be discretized over this mesh.

Constant density, but not speed of sound, is assumed throughout the column. Using the notation $\Psi_j = \Psi(z_j)$, the Taylor series expansion of Ψ is obtained

$$\Psi_{j+1} = \Psi_j + \Psi'_j h + \Psi''_j \frac{h^2}{2!} + \Psi'''_j \frac{h^3}{3!} + ..., \tag{2.36}$$

with prime denoting differentiation with respect to z. This expansion can be rearranged to obtain a forward difference approximation of the first derivative,

$$\Psi'_j = \frac{\Psi_{j+1} - \Psi_j}{h} - \Psi''_j \frac{h}{2} + ..., \tag{2.37}$$

which can be truncated to a first order approximation,

$$\Psi'_j \simeq \frac{\Psi_{j+1} - \Psi_j}{h}. \tag{2.38}$$

A second order approximation is obtainable by substituting into the modal equation, 2.24,

$$\Psi'_j \simeq \frac{\Psi_{j+1} - \Psi_j}{h} + \left[\frac{\omega^2}{c^2(z_j)} - \xi^2\right] \Psi_j \frac{h}{2}. \tag{2.39}$$

Using a similar method results in the backward difference approximations

$$\Psi'_j \simeq \frac{\Psi_j - \Psi_{j-1}}{h}, \tag{2.40}$$

and

$$\Psi'_j \simeq \frac{\Psi_j - \Psi_{j-1}}{h} - \left[\frac{\omega^2}{c^2(z_j)} - \xi^2\right] \Psi_j \frac{h}{2}. \tag{2.41}$$

Finally, the combination of the forward and backward difference formulations yields a centered difference approximation of the second derivative,

$$\Psi''_j \simeq \frac{\Psi_{j-1} - 2\Psi_j + \Psi_{j+1}}{h^2}. \tag{2.42}$$

Recalling the continuous modal equation and its boundary conditions,

$$\Psi''(z) + \left[\frac{\omega^2}{c^2(z)} - \xi^2\right] \Psi(z) = 0, \tag{2.43}$$

$$A_1 \Psi(0) + B_1 \frac{d\Psi(0)}{dz} = 0, \tag{2.44}$$

$$A_2 \Psi(D) + B_2 \frac{d\Psi(D)}{dz} = 0, \tag{2.45}$$

it is now possible to use the difference approximations to obtain a series of difference equations for the water column. These difference equations are collected to form an

algebraic eigenvalue problem of the form $\mathbf{A}(\xi^2)\mathbf{\Psi} = 0$, where $\mathbf{\Psi}$ is the vector of the approximations of the eigenfunctions evaluated at the mesh points $\Psi_0, \Psi_1, ..., \Psi_N$. $\mathbf{A}$ is the coefficient matrix defined by

$$\mathbf{A} = \begin{bmatrix} d_0 & e_1 & & & & & \\ e_1 & d_1 & e_2 & & & & \\ & e_2 & d_2 & e_3 & & & \\ & & \ddots & \ddots & \ddots & & \\ & & & e_{N-2} & d_{N-2} & e_{N-1} & \\ & & & & e_{N-1} & d_{N_1} & e_N \\ & & & & & e_N & d_N \end{bmatrix}, \tag{2.46}$$

with

$$d_0 = \frac{-2 + h^2[\omega^2/c^2(z_0) - \xi^2]}{2h\rho} + \frac{A_1}{B_1}, \tag{2.47}$$

$$d_j = \frac{-2 + h^2[\omega^2/c^2(z_0) - \xi^2]}{h\rho}, j = 1, ..., N-1, \tag{2.48}$$

$$d_N = \frac{-2 + h^2[\omega^2/c^2(z_0) - \xi^2]}{2h\rho} + \frac{A_2}{B_2}, \tag{2.49}$$

$$e_j = \frac{1}{h\rho}. \tag{2.50}$$

This matrix is solved using the TNT matrix libraries eigenvalue solution routines[28], yielding discretized approximations to the eigenfunctions and eigenvalues. These are then used with equation 2.35 to solve for the transmission loss of the domain. As with the equation model, the difference between the transmission loss predicted by the normal mode model and that predicted by spherical spreading is taken, and added to the original spectrogram. Figure 2.7 shows the process flow diagram, including all three propagation models, for the entire solution to the hydrodynamic hull noise problem.

2.3 Chapter Summary

As fluid flows through a medium, disturbances caused by turbulence within the flow can be transformed into acoustic energy which can propagate throughout the medium as sound. The generation of sound in a free fluid flow can be described as a distribution

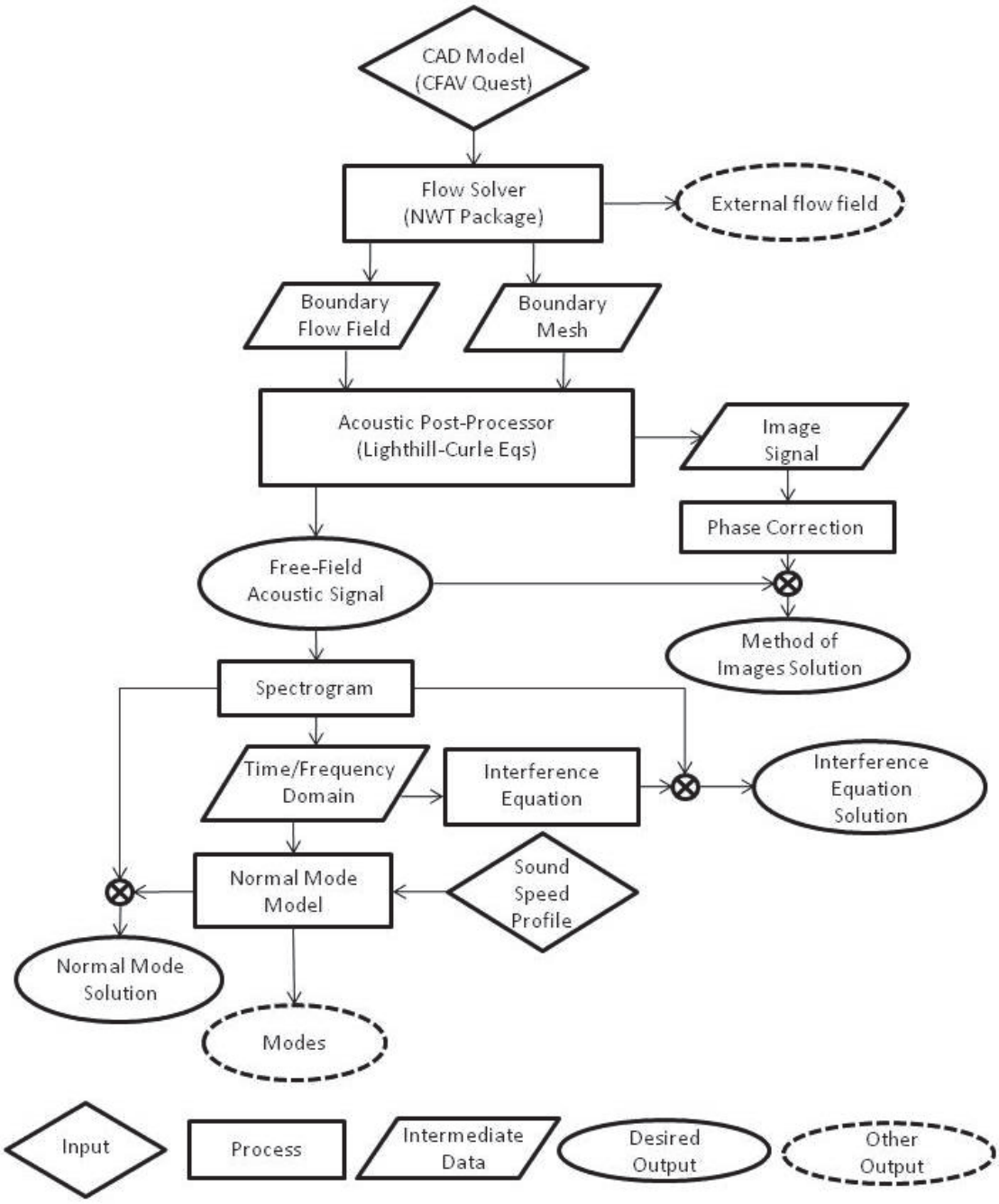

Figure 2.7: Process flow diagram for the hydrodynamic hull noise simulation problem

of quadropole sources according to Lighthill's equation for aerodynamic sound. In the presence of solid boundaries, such as along the hull of a ship, this sound generation is better described as a distribution of dipoles along the solid boundary, as per Curle's equation. The efficiency of the conversion from flow energy to acoustic energy is much greater in dipoles, and so they dominate at low Mach numbers, such as flow around a ship hull.

In more complex flow environments, different effects can alter the propagation of acoustic energy into the field far from the source. These effects are best described as transmission losses, and are often above and beyond the loss due to spherical spreading that is predicted by the Lighthill-Curle equation. In the presence of the sea surface, the dominating effect is the generation of Lloyd's Mirror interference. It is caused by reflections of sound from the sea surface arriving at a receiver and interfering with sound signals that arrived directly from the source.

Three different methods of simulating this transmission loss have been described, each utilizing different simplifying assumptions. The equation for the Lloyd's Mirror loss of a simple, acoustically compact source assumes that the source is small compared to the wavelength of sound which is produces, which cannot be guaranteed for the broadband noise produced by a ship in motion. The method of images solution utilizes the principle of superposition to solve for the total response of the ocean to both the real ship and a Lloyd's Mirror image ship, but assumes that the ocean is a linear system. Finally, normal mode models calculate the response of the vertical water column to excitations caused by the acoustic source, in the form of a set of normalized modes. These modes are then propagated into the far field according to their mode number. The complex interaction of these modes will capture both the effects of sea surface reflections and the varying properties of the vertical water column, eliminating the linearity assumption. All three models have been implemented into a Lighthill-Curle acoustic post processor and will be compared for their ability to accurately predict the sound generated by CFAV Quest in at-sea trials.

Chapter 3

Validation of the Bow Pressure Field Fluctuations

The nature of the simulation process is such that each consecutive model builds on the output of the previous. The accuracy of the first stage, the modeling of fluid flow, is therefore critical to the success of all later stages of modeling. Errors introduced into the process here will propagate throughout the subsequent results of the simulation, and it is vitally important to understand and control the sources of error at this level. Previous efforts to validate the NWT for use with an acoustic post-processor used benchmark results for the lift and drag characteristics of the flow around a cylinder. While such simple shapes give good insight into the capabilities of CFD tools like NWT, extrapolating the accuracy from that to the model of a ship such as CFAV Quest is a large step.

In order to further validate the NWT as an acoustic simulation tool, experimental data from the actual ship was required. During at-sea trials of CFAV Quest, dynamic rangings were conducted with a series of pressure sensors mounted to the bow of the ship. The recorded hull pressure fluctuations are here compared to those simulated by the NWT, in order to assess NWT's ability to accurately predict hull pressure. Recalling equation 2.7, hull pressure is one of the components of the Lighthill stress tensor source term for sound generation. This chapter will present the results of that comparison, and will go on to discuss the sources and significance of error in the simulated hull pressure field.

3.1 Simulation and Experimental Sea Trials Data

Experimental data on the hull pressure fluctuations of CFAV Quest was collected during a dynamic acoustic ranging outside of Halifax. Repeated north-south runs were conducted in level flight with the ships engines held at constant RPM. Sea state and wind speed were both low enough to be considered negligible. Hull pressure data was sampled at 25 kHz, and logged and filtered by DRDC staff. Figure 3.1 shows the

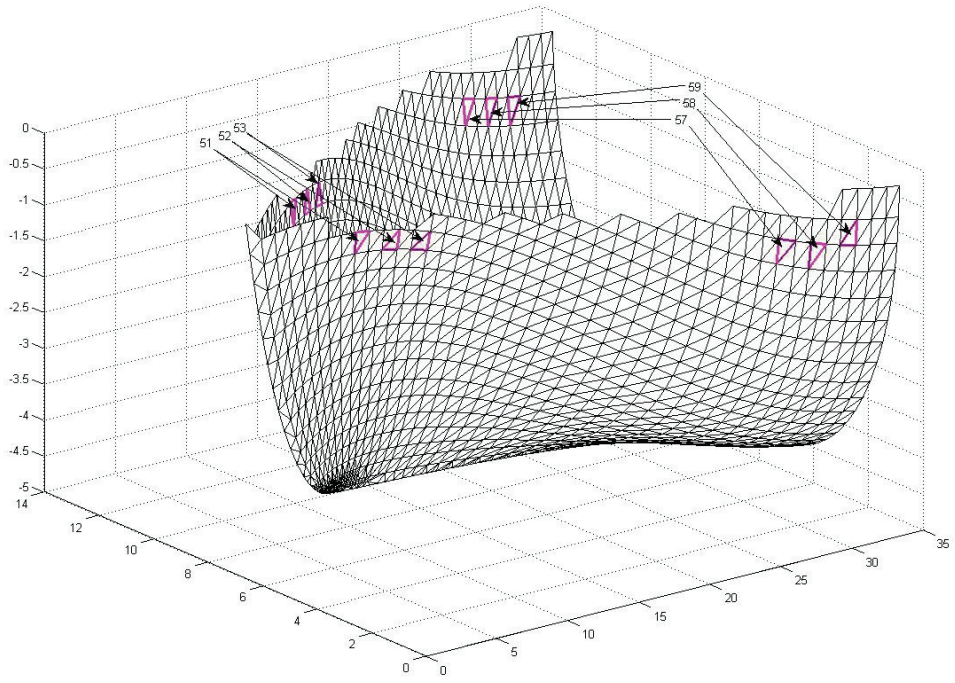

Figure 3.1: Schematic diagram showing the location of hull pressure sensors on CFAV Quests bow

STL model of CFAV Quest used in simulations, with the location of the mounted hull sensors highlighted and named in order from bow to stern: 51, 52, 53, 57, 58, and 59. In this figure, the design waterline corresponds to 0 on the z axis. It is important to note that the aspect ratio of this figure is not to scale. Further details on the ranging setup and conditions are available in the Chief Scientists log [1] and cruise plan [2].

For this study, only the bow half of the ship has been modeled. This is in keeping with the methodology used by Murphy in [23]. An artificial end cap has been added which is not shown in figure 3.1, the prevent any flow from entering the interior of the model. This choice was originally made to save computation time by reducing the computational domain, and in recognition of the relative contribution of the hydrodynamic hull noise on the bow to the ships signature as heard at the SONAR dome. It has been continued hear for the same reasons, and to maintain comparability between this work and that of Murphy. Impacts of this simplification will be elaborated on in section 3.3.

For numerical purposes, the ship model was scaled down by 10, while flow speed was scaled to unity. The simulation Reynolds number, based on the ships beam, is matched with experiment by adjusting the simulated fluid's kinematic viscosity. Reynolds numbers similitude is important to maintain in order to ensure that the balance of inertial and viscous forces in the simulation matches experimental conditions. This balance will govern a variety of flow properties, including but not limited to boundary layer thickness, turbulent length scales, and viscous dissipation. Due to the heavy interaction between flow acoustics and flow turbulence, Reynolds number similitude is essential to a good acoustic solution.

Approximately 350,000 cells are used to define the domain, which has Neumann boundary conditions at the inlet, Dirichlet at the outlet, slip conditions on the sides, and no-slip at the ships hull. The grid is continuously adapted as per the NWT's grid adaptation algorithms (see [6]); a sample grid is included in appendix C. The simulations were developed for ten seconds to ensure a quasi-steady state, and then acoustic source data was recorded for seven seconds. The time step is held constant at 0.0015 seconds. Time step size will be inversely proportional to frequency resolution, but directly proportional to simulation run time. While higher frequencies are preferable, hardware and run time limitations are unavoidable. This time step was chosen to balance these contradicting needs, giving a maximum resolved frequency of 333 Hz, with a run time on the order of several months.

Table 3.1 lists the simulated ship speeds, Reynold's number, experimental engine RPM, and the corresponding target experimental ship speeds. The reader will note that the target ship speeds do not precisely match the simulation speed. In experiment, the ships engines were run at a constant RPM so as to reach the target velocity and maintain a constant power output. Measurements of actual ship velocity through water are not available, and so the RPM and target velocities represent approximations only. Quasi-semi state flow solutions were available at four and six knots prior to receiving experimental data. Due to the time required to develop steady state data, several months of simulations, the choice was made to accept the velocity mismatch. The impact of this decision will be elaborated upon in section 3.3.

Simulation Speed (knots)	Reynolds Number	Engine RPM	Target Experimental Speed (knots)
4	1.79E8	30	3
6	2.60E8	60	6

Table 3.1: Simulated and corresponding experimental conditions

3.2 Hull Pressure Comparisons

The simulated pressure signals corresponding to the hull sensors were extracted from the acoustic source data for comparison with the data obtained from the trials. The trials data contained only the fluctuating component of pressure; the signal had 0 mean. As such, the NWT data has also had its mean value removed. Figure 3.2 gives a comparison of RMS pressure fluctuation for each sensor at all ship speeds. Here, dark blue and light blue represent north and south bound trial runs of CFAV Quest respectively. Since the simulated sea state is assumed calm with no ambient convection, the ships bearing will have no effect on simulations. North and south bound runs therefore cannot be distinguished within NWT, and so in order to arrive at two signals for comparison, port and starboard signals from the simulated ship are used. Here, red represents a port signal, and green a starboard signal. Since DRDC logs are ambiguous as to which side of the ship recordings were taken on, both are shown. This convention and reasoning is followed for every subsequent comparison. Marker type here indicates the ship speed. For the readers convenience the sensor points in a related run have been connected, but this should not be taken to indicate a continuous or streamline flow from sensor to sensor. The difference between the averaged simulation and experimental results is also plotted, and is shown in percent error, here defined as $\frac{|Experimental-Simulation|}{Experimental}$.

It can be seen that the error of RMS predictions decreases along the length of the ship, to a minimum at sensor 57, and then increases rapidly again through sensors 58 and 59. With the exception of the 4 knot north-bound case at sensor 57, the simulations under-predict the RMS fluctuation at every sensor. Furthermore, the error is proportional to ship speed, with four knots having a lower error at all sensors and a dramatically lower minimum error of 10%, compared to 85% at six knots.

For a more detailed analysis of the simulation and trials data, the signals must be converted into the frequency domain. A time step size of 0.0015 s is equivalent to a

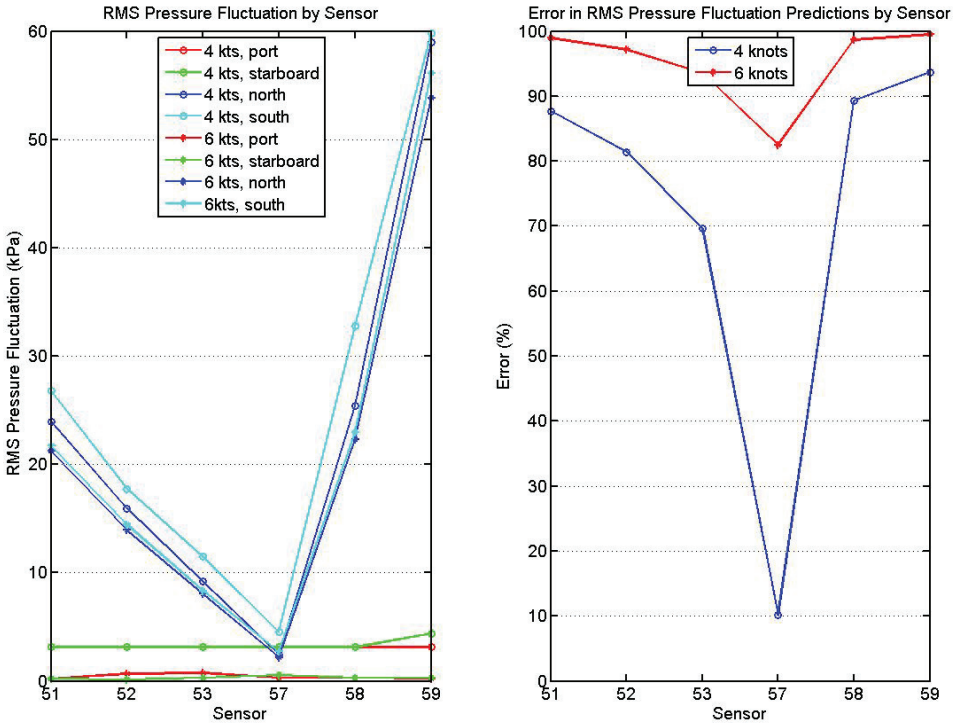

Figure 3.2: RMS pressure fluctuations for each sensor at varying ship speeds

Nyquist frequency of 333 Hz. In simulation, recall that the ships beam is scaled to 1.26 m, and the velocity held constant to 1 m/s. Again taking the ship's beam as the characteristic length, with Strouhal number defined as:

$$St = \frac{fl_0}{u_0}, \tag{3.1}$$

the simulated range of Strouhal number will lie between 0 and 420. Trials data is available up to 12.5 kHz, with a beam of 12.6 m and ship speeds at four and six knots. Table 3.2 gives the corresponding frequency limit for a Strouhal number limit of 420. Spectrum estimates of all signals have been obtained from Welch's method, using 8 Hamming windows at 50% overlap. For more information on Welch's method, see appendix A or [25].

Figures 3.3 and 3.4 show these spectrum estimates for each of the six sensors at the four and six knot simulation speeds respectively. The trials results clearly show a decrease in spectral power with increasing frequency, while the simulation results show a more uniform distribution in power across the spectrum. It should be noted

Ships Speed (knots)	Maximum Frequency (Hz)
4	68.53
6	102.8

Table 3.2: Maximum comparable frequency from a limiting Strouhal number of 420

that while the power appears constant in the four knot case it is in fact varying, on average by $\pm 1dB$.

It can be seen that in all cases, the simulations perform better in the high Strouhal number range. Best results are obtained in the band over $St = 200$. Simulation results also fail to replicate local peaks of spectral energy, such as those shown at $St = 175$ and $St = 300$ in Sensor 51, six knots.

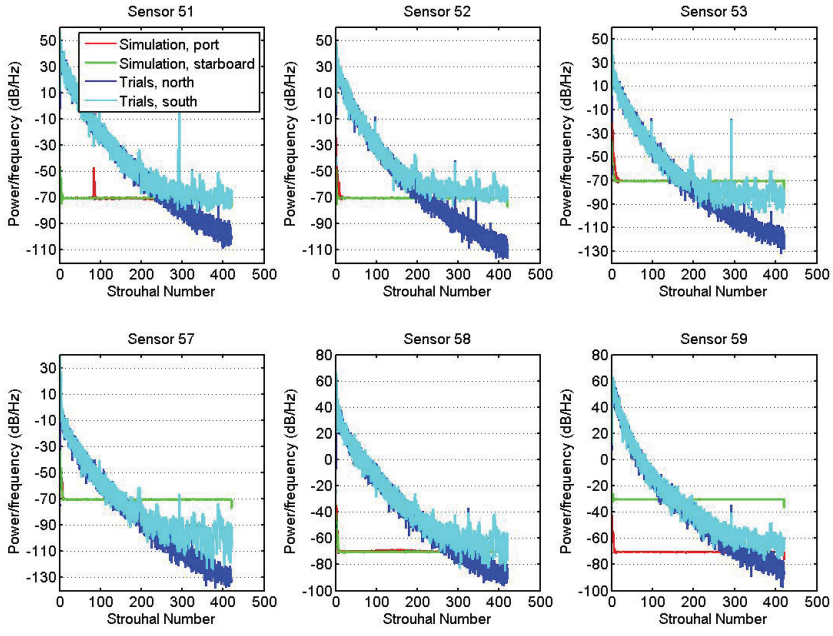

Figure 3.3: Hull pressure spectrum estimates, 4 knots

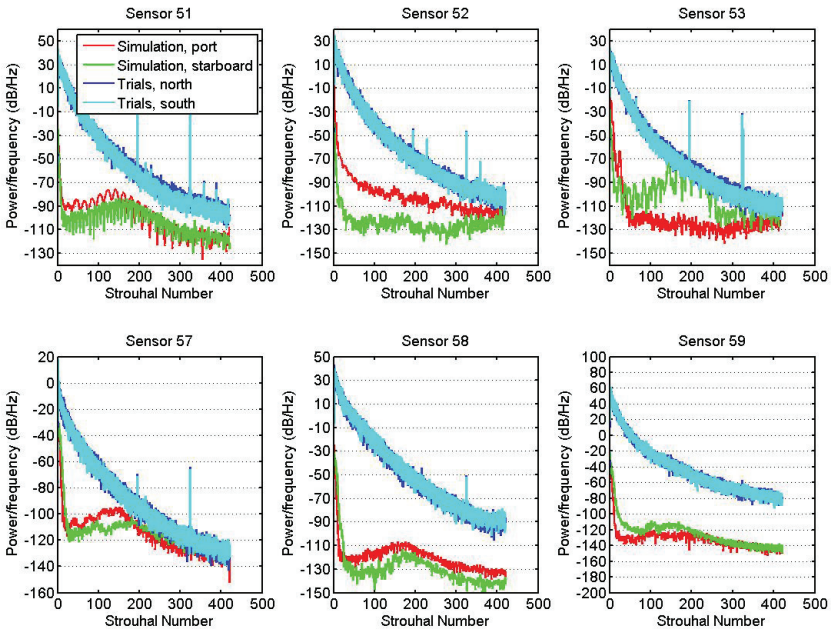

Figure 3.4: Hull pressure spectrum estimates, 6 knots

Figure 3.5 gives the averaged simulation error as a function of frequency for each ship speed at each sensor. This value was obtained by taking the difference between the average of the two trials signals (north and south) and the average of the two simulation signals (port and starboard). Figure 3.6 takes this data and averages it across the range of Strouhal numbers to arrive at a single averaged error value for each sensor. This averaging was done without regard to phase, and so does not take into account temporal variation of the error. In this way, the spectrum estimates are assumed to be constant with time, which has not been definitively shown. It is possible that a spectrographic analysis, which accounts for both phase and frequency of the error, would provide a more detailed description of the spectral error. Time restraints prevented such a detailed analysis. Figure 3.5 demonstrates the inverse relationship between Strouhal number and error, with the vast majority of the error in the low Strouhal number range. From figures 3.5 and 3.6 it can be observed that the error is also again dependent on ship speed and sensor location, with error reaching a minimum in the mid-bow region and at the lower ship speed.

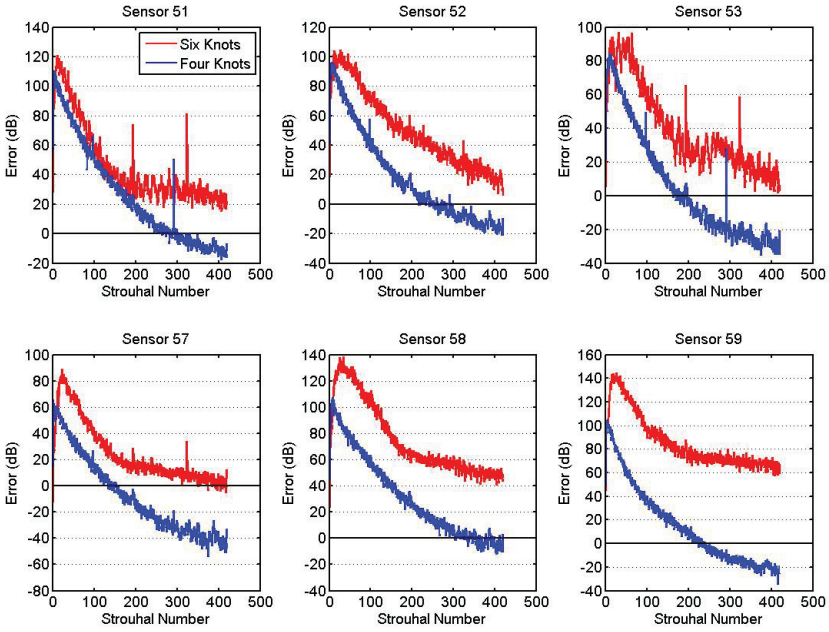

Figure 3.5: Averaged pressure spectrum error, by sensor and speed

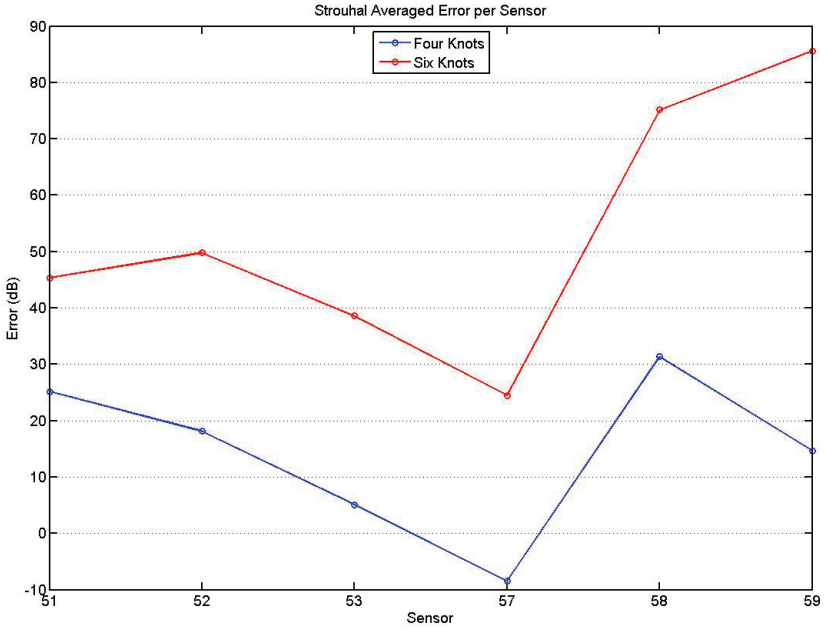

Figure 3.6: Frequency averaged power spectral density error

3.3 Discussion

3.3.1 Sources of Error

Extrapolating the results of six pressure sensors mounted on the ship's bow to the entire pressure field along the hull is at best problematic. While a greater resolution of the pressure field is desirable, collecting data from sea trials on an actual ship is a prohibitively expensive method for verifying the accuracy of the simulated pressure field.

By examining the simulated pressure field for the entire bow of the ship, it is possible to compare the simulated sensor results to the entire fluctuating field. Figure 3.7 shows the RMS pressure fluctuations at 6 knots, mapped along the ship's bow half and highlights the location of hull facets corresponding to sensors. These are simulated results, and so the accuracy of their predictions is ambiguous. It can be seen that the NWT predicts that the three bow-most sensors (51, 52, and 53) are located in an area of high pressure fluctuation, while the stern sensor fluctuations (57, 58, and 59) are closer to the mean fluctuation across the bow. The two sternmost sensors, 58 and 59, consistently had the highest simulation error, and the suggestion of figure 3.7 that they are closest to the mean and therefore most typical of the sensors further reinforces the possibility that the entire pressure field may be in error. The results of figure 3.7 are typical of both simulated ship speeds, the plots for which are reproduced in appendix C.

The results of comparison with trials data clearly shows significant error in the low Strouhal number ($St < 200$) range. This error also increases as a function of ship speed. If the sensor results can be taken as typical of the pressure field on the bow of the ship, the pressure fluctuations then represents a potentially significant source of error introduced at the early stages of the simulation process.

For the purposes of discussion, the potential sources of error will here be divided into three broad categories: those introduced by simulation, by experiment, and by signal processing. Simulation errors will here mean those errors introduced in the CFD simulation process, and are thus only relevant to simulation results. Experimental errors, conversely, are those that are introduced in the collection of experimental data during at sea trials and pertain to trials data only. The distinction is important

because the third category, signal processing errors, potentially impacts both simulation and trials data sets, and relates to errors and uncertainty caused by the signal processing techniques applied.

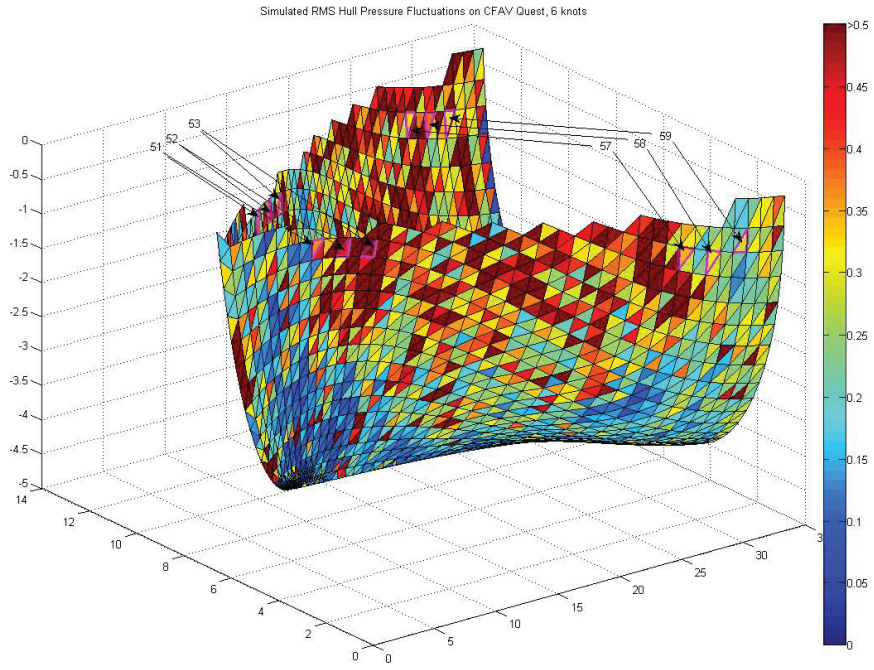

Figure 3.7: Map of simulated RMS pressure fluctuations along the hull of CFAV Quest at 6 knots

Simulation Error

The numerical nature of CFD simulations necessarily involves approximation and error. Wherever possible, these have been limited to increase the utility of the simulation results, however they can never be completely removed. Errors in CFD are often furthered classified into modeling errors, which can be thought of as the difference between the real flow and the the mathematical equations being used to describe it, discretization errors, which are the result of discretizing the exact equations, and iterative errors, which are the result of iteratively solving the discretized equations.

The iterative error of the solutions is known, with convergence of the solution being assumed after achieving a residual of $1e-5$ for velocity and $1e-6$ for pressure.

Previous work with the NWT package has shown that the discretization error is problem dependent, typically on the order of Δx^2. A more exact figure in terms of dB error could be obtained through a grid convergence study, wherein progressively smaller CFD grids are simulated and the resulting error in the acoustic predictions is quantified. Time restrains prevent the undertaking of such a study, however it is a recommended step in future research.

Three potential sources of modeling error exist in this simulation methodology. The NWT is currently incapable of modeling the free ocean surface, or any effects associated with it. Neglecting the ocean surface not only effects the transmission of sound and is the motivating factor for this study, but will also impact the flow simulations themselves. The relative importance of free surface effects can be qualitatively described by the Froude number,

$$Fr = \frac{V}{\sqrt{gl}}, \tag{3.2}$$

which measures the ratio of inertial forces in a flow to gravitational forces. Again the characteristic length l is taken to be the ships beam. Along with the Reynolds number, the Froude number is used as a measure of the expected resistive forces felt by a ship in motion. The Froude number here is 0.28 for the 6 knot case, and 0.18 for the 4 knot case. Where the primary resistive mechanism attributed to the Reynolds number is skin friction, the biggest, and certainly most visible, mechanism attributed to Froude number dependence is the generation of the bow wave.

Any ship in motion will generate a wave train, starting at the bow of the ship. This wave will have a significant effect on the resistance or drag felt by the ship, and will dramatically alter the character of the pressure field on the ship [21]. While predicting the exact height and energy of the bow wave is a complex topic in itself, a large factor for both will be the ships velocity, as denoted by the Froude number. Simple bow wave analysis takes the wavelength of the produced wave to be $\lambda = \frac{2\pi V^2}{g}$ with its origin at $\frac{\lambda}{4}$. Taking this value as the wave origin would locate the wave within 5 m of the forward perpendicular at all speeds in our simulation, and within 10 m or 2 wavelengths of the forward sensors.

In addition to the presence of the bow wave, a free sea surface would itself require alternative boundary conditions to those in the simulated flow. In the absence of surface tension effects, which can be safely neglected at these length scales, the free

surface boundary condition is often taken as a pressure matching boundary condition. This condition would require the pressure in the liquid water flow to be matched with the air pressure at the oceans surface. The calculation is complicated by the requirement to calculate the location and velocity of the free surface, which would be non-constant. The location of all six simulated sensors are close to the ships waterline, within 1 m, which has here been modeled as a simple slip boundary condition. Slip boundaries do not prescribe a pressure at the boundary, and instead only require flow tangency. The boundary condition is therefore not guaranteed to match real-world conditions, nor is it guaranteed to be located in the correct location.

While an exact analysis is not possible, it is worth noting from figure 3.7 that the current simulation results predict large pressure fluctuation near the boundary. A more physically accurate pressure boundary condition in that region would likely have a significant impact on the local pressure field.

In addition to neglecting the generation of the bow wave and the incorrect free surface boundary condition, the ship itself has been approximated using only the bow half. The growth and separation of the turbulent boundary layer is dependent on the gradients of pressure which develop along the length of the ships hull. By neglecting the rear portion of the hull, those gradients will be increasingly in error as mid-ship region is approached. As a result, the boundary layer thickness and the turbulent variables at the rear of the ship will be less accurate. Furthermore, the cut in the ship will effectively create a wake with turbulent wake dynamics at the mid ship, where it would not physically exist. This may feedback onto the ships hull ahead of the cut, causing a further loss of accuracy in that region. It was seen that the worst comparisons between experimental and simulated results were obtained at sensors 58 and 59, located close to the cut plane. This may be partially explained by the lack of the ships stern half.

The third major source of potential modeling error is the turbulence model. As mentioned in chapter 1, the NWT uses a hybrid of the Smagorinsky LES model and the Baldwin-Lomax mixing length model. LES models spatially filter the fluid flow, directly calculating those turbulent fluctuations above the filtering length. Fluctuations below the filtering length are not directly resolved, rather their effect is modeled using a sub-grid scale (SGS) model. LES models give good results for free flows and

separated flows, however they give poor results for the flow closest to solid surfaces. This tendency to poorly predict near-wall values is due to the fact that they do not directly calculate the small scale motions that dominate in the near-wall region[7].

Despite this limitation, LES models are important because they can give time variant turbulence solutions. Alternative models make use of Reynolds averaging (RANS) methodologies and only report time averaged turbulence quantities. Sound generation is by nature a time variant quantity, and LES models are therefore more appropriate. There remains the issue that the near-wall turbulent parameters are extremely important to the generation of sound.

The hybrid Baldwin-Lomax Smagorinsky, or BLS, model was developed to attempt to address this issue. The Baldwin-Lomax model is a RANS model, and is used to supplement the SGS model of the standard Smagorinsky model. It calculates the sub-grid eddy viscosity based on a mixing length, and so is referred to as a mixing length model. The hybrid model was shown to give improved simulation results over either Baldwin-Lomax or Smagorinsky models by themselves, as well as being able to handle both seperated flows and flows with significant near-wall features[7].

Research has shown however that while such methods can give improved results for near-wall flow, the turbulent structures that appear in such flow are often not physically realistic and the values can still not be viewed as accurate in all cases. The Baldwin-Lomax and other RANS models are all dependent on a set of calibration statistics, which will have significant effects on their turbulent flow[24] [31]. Baggett also shows in [5] how the artificial separation of scales in a hybrid LES and RANS model can lead to the generation of spurious turbulent structure when combined with the no-slip boundary condition. In brief, it is shown that the RANS models must artificially inflate the turbulence in order to properly communicate the boundary condition through the near wall region. While this may not be a concern for large scale flow features it will lead to inaccuracy for quantities in the near wall region, such as the fluctuating pressure on the hull of a ship.

While the hybrid model is an improvement compared to the Smagorinsky LES model alone, there are many reasons to doubt its accuracy. Near wall flow features are of primary concern for the generation of acoustic energy. Furthermore, the tuning parameters used in this model have not been calibrated for this specific use, but rather

are those most commonly used in literature. Wilcox points out in [31] that mixing length models such as Baldwin-Lomax are especially in need of tuning, and are very difficult to extrapolate out of the cases they have been tuned for. For these reasons the turbulence model can here be taken as a significant potential source of modeling error.

Experimental Error

Errors introduced by the experimental setup of the at-sea trials are difficult to ascertain due to the independent collection of that data. It is known that DRDC technicians filtered the pressure data, however details of the filters used are not known to the author as of this writing. Similarly, details on the make and installation of the pressure transducers used are not known. The operating range of the pressure sensors is reported in the Chief Scientist's log[1] as per table 3.3.

Sensor	Operating Range (± kPa)
51	250
52	252
53	193
57	183.9
58	315.2
59	198.3

Table 3.3: Experimental sensor operating range

Of particular note in examining the experimental data is the fact that the exact ship speed is neither controlled nor recorded. As was mentioned above, and listed in table 3.1, the engine's RPM was kept constant in order to achieve a desired speed through water. While the engine RPM was controlled, there is no record of whether the desired ship speed through water was attained or held. It is likely that the ship underwent fluctuating accelerations about an average speed that may or may not have been the desired one. Conversely, the CFD simulation process maintains an exactly constant ship speed as per table 3.1.

On examination of that table, it is also clear that the target ship speed and simulation speed do not always match, as is the case for four knots. The reason for this mismatch is that, at the indicated speed, semi-steady state data was already available. Eliminating the requirement to advance a simulation to the steady state condition

significantly reduces the computational time. Due to the uncertain nature of the trials data ship speeds, the loss of accuracy resulting from this mismatch of simulated and experimental data was deemed acceptable in exchange for the considerable time savings.

Without knowing details of the ship's velocity through the water, it is difficult to quantify the impact of this error. Average error in spectral estimates does appear to be proportional to ship speed by a factor of approximately 12 dB/knot, or 24 dB/$\frac{m}{s}$. A fluctuating acceleration compounds the problem by making the ship speed non-constant.

Signal Processing Error

Signal processing techniques were, wherever possible, kept identical between trials and simulation data. This matching was done with the intention that any error introduced as a result of the bias or variance of the technique would be matched between both sets of data. The higher sampling frequency and signal length of the trials data will naturally result in much greater resolution of the spectral content of the trials signals. In all spectrum estimation techniques, the accuracy of the final estimate will always be proportional to signal length, and the trials data will thereby always yield a more accurate estimate.

Nevertheless, significant error can be present in the spectrum estimates of both experimental and simulation data. While the use of Welch's method reduces the bias and variance of spectrum estimates compared to the periodogram, it does not remove it. Furthermore, because Welch's method still ultimately relies on the Fourier transform to obtain spectral data, it is subject to the well known problem of Gibbs phenomenon.

Gibbs phenomenon is the name given to the behavior of the Fourier series around discontinuities. In spectral estimation, the finite signal being examined is assumed to be cyclical with a period equal to its signal length. This assumption results in discontinuities at the ends of the signal. When the Fourier transform of this signal is taken, false oscillations will be introduced at the ends of the estimated spectrum. The error from these oscillations can be reduced in spectral width and energy by increasing the signal length, but they cannot be removed without modifying the

Fourier transform. Since frequencies over the Nyquist limit are of no interest due to aliasing, this effect will only impact low frequency data. While the effect of this error can be significant it is difficult to quantify for complex signals. The use of 8 Hamming windows at 50% overlap in the Welch spectral estimate was done in an attempt to limit the impact of this error on the estimates. It is possible that alternative parameters for window shape, length and overlap could yield better spectral power density estimates, however an in-depth study of the signal processing methodology is beyond the scope of this study.

The presence of Gibbs phenomenon is more obviously seen in the very low frequency behavior of the simulation results. The sharp increase of power seen in all estimates as they approach zero is due to Gibbs effects. Due to the gradual increase in power with lower frequency seen in the trials data, it is difficult to say how much of an impact Gibbs phenomenon has. Since the signal lengths of the trials data is much larger than simulation, it is likely that the impact is greatly reduced. While more advanced signal processing techniques are available to help mitigate the impact of this effect, they are beyond the scope of the current work. Gibbs phenomenon remain an important source of error at very low frequencies, due to the significant error found in the low frequency region where they exist.

3.3.2 Sensitivity to Pressure Error

While the presence of error in the hull pressure fluctuation predictions at the bow is a concern, it is important to remember that the overall goal of this modeling process is not the prediction of bow pressures. The varying pressure field on the hull of the ship is one of two factors in the generation of hydrodynamic noise, with the other being the viscous stress tensor on the surface. While errors in the pressure calculated at the CFD stage of the simulation process will propagate throughout the entire simulation, the effect they have on the final acoustic prediction is difficult to predict. Without experimental data on the surface stress, it is impossible to determine the accuracy of that quantity. Errors in the pressure data are not necessarily indicative of errors in the flow velocity data on which the stress tensor is based; it is possible that the CFD process is accurate for one but not the other.

Figure 3.8 shows the sound pressure levels as predicted for six knot simulations

with modified pressure signals. The blue line represents the un-altered SPL, without including any sea-surface effects, while the red, green and magenta lines respectively represent a 10, 20 and 30 dB alteration to the pressure signal at all points. The resulting shift in predicted SPL is seen to be almost double the shift in the input pressure signal. It is important to note that the pressure signal error is not distributed uniformly across the frequency band, nor is it uniform across the hull, and so a frequency independent shift at all points is at best a poor indicator of its character. Nevertheless, the result does show a significant effect on the final SPL prediction. Table 3.4 gives the approximate error for each simulation speed, averaged across frequency and sensor. It can be seen that for all simulation speeds a frequency independent error can be reasonably assumed.

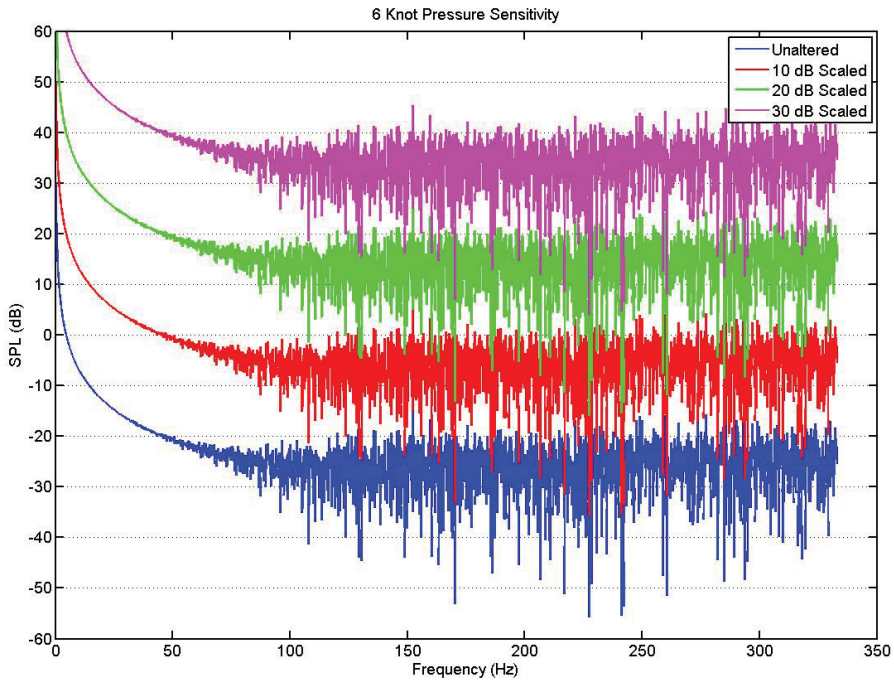

Figure 3.8: Plot of simulated SPL from unmodified and altered pressure signals

Speed (knots)	Error (dB)
4	14.32
6	53.15

Table 3.4: Averaged simulation error

3.4 Chapter Summary

The results of experimental data collected during at-sea trials of CFAV Quest were compared to the simulated data. Simulated data was shown to under-predict the RMS pressure fluctuation by a varying but significant margin that increased with the speed of the ship. Spectral analysis revealed that the majority of the error was confined to the low Strouhal number range ($Str < 200$). Results above $Str = 200$ were increasingly accurate. Results below $Str = 200$ diverged significantly, with error ranging from 20 dB to 140 dB. Error was also shown to be spatially distributed, with those sensors located at the fore and aft extremes of the simulation showing higher error.

Two potential sources of modeling error were identified. The NWT is incapable of modeling the generation and flow effects of the wave found at the bow of a ship in motion. This wave can have a significant impact on the local pressure field in the bow, but a quantitative analysis of the error associated with its neglect is not possible at this time. Additionally, the turbulence models used in the NWT are known to give both physically and numerically inaccurate results in near-wall regions, such as the pressure fluctuation on the ships hull, and are sensitive to problem specific tuning parameters. These parameters have not been investigated for this application, instead a general set has been implemented.

Two potential sources of experimental error were identified. The pressure signals have been filtered using an unknown process, and the accuracy of this filtration cannot be assessed. The ship's exact speed is not known and likely non-constant, and experimental target ship speeds are known to not match the simulation ship speed in all cases. This velocity mismatch constitutes a major potential source of error, since error was shown to be strongly velocity dependent. Time restraints prevented generating additional simulation data to match the experimental velocity.

The pressure fluctuation's average broadband error for all sensors was shown to be 14.32 dB at four knots and 53.15 dB at 6 knots. A simple sensitivity analysis showed that if this error is assumed for the entire pressure field, a proportional error can be expected in the acoustic prediction. Chapter four will present the results of acoustic predictions and discuss their accuracy in greater detail.

Chapter 4

Acoustic Simulation Results

The first and most important goal of this project is the accurate prediction of the hydrodynamic hull noise as heard by a hydrophone located close to the sea surface. As was discussed in section 2.2, simulations done without including the effects of the free sea surface are physically inaccurate, and the results produced by Murphy in [23] over-predicted sound pressure levels (SPL). Three different propagation models have been constructed to include the Lloyd's Mirror effect, the dominant effect of the sea surface. This chapter begins by verifying the Lloyd's Mirror models implemented in the post processor against the results published by Pederson in [26][27]. The conditions of the at-sea trials of CFAV Quest, and their simulation setup will then be discussed, followed by a comparison of the simulation and experimental results.

4.1 Lloyds Mirror Validation

The propagation models were chosen for their ability to realistically model the Lloyd's Mirror effect of the sea surface for a complex source. It remains to be seen, however, with what degree of accuracy the implemented models are able to reproduce the character of Lloyd's Mirror interference. To this end, the simplified and normal mode models have both been run in identical Lloyd's Mirror conditions, and compared against results from literature. The method of images solution requires a detailed solution in the time domain, as opposed to the spectral methods used by the simplified and normal mode models. Time restraints on this project therefore prevent a Lloyd's Mirror validation from being carried out on the method of images solution.

Models were validated against data collected by Pederson, as presented in [27] and [26]. In brief, a simple source, transmitting at 1030 Hz, was towed at a depth of 55 ft across a 10 kyd range with a hydrophone recording at 50 ft depth. The source was pulsed at specific intervals to create a set of ranged data points that reveal the distinctive pattern of Lloyd's Mirror interference. The water column was

modeled as a bi-linear gradient, given by equation 4.1. The tuning parameters were found by bathymetry measurements, and their mean values were taken to be $C_0 = 4940.87 ft/s, z_a = 320 ft, \gamma_0 = 0.0144 s^{-1}$,and$\gamma_1 = -0.431 s^{-1}$.

$$C(z) = \begin{cases} \frac{C_0}{\sqrt{1-2\frac{\gamma_0}{C_0}Z}}, & z < z_a \\ \frac{C_0}{\sqrt{1-2\frac{\gamma_0}{C_0}z_a - 2\frac{\gamma_1}{C_0}(z-z_a)}}, & z > z_a \end{cases} \tag{4.1}$$

These conditions were replicated in the acoustic post processor for the simplified source and normal mode models. Figure 4.1 gives the results, along with a visual representation of the bi-linear sound speed gradient. The blue line here represents the results for the simplified equation, the red the normal mode model, and the violet points the experimental results of Pederson. The green line shows the results of neglecting Lloyd's Mirror interference over that range, as per the original model; it is simply the expected transmission loss from spherical spreading.

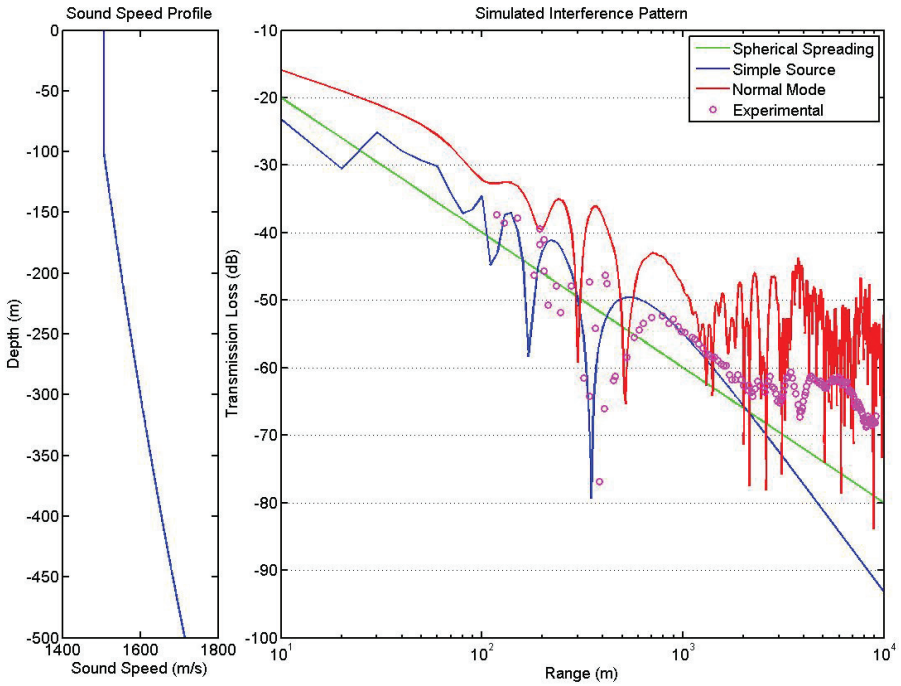

Figure 4.1: Sound speed gradient and Lloyd's Mirror interference fields for a 1030 Hz signal. 50 ft source depth, 55 ft receiver depth

As per Pedersons work, only the first 40 modes have been used in the normal mode

model. These modes have been sampled at 4 samples/m. Theoretically, including more modes would yield a solution of greater accuracy, at the cost of computation time. One must be careful to avoid aliasing in the higher order modes; aliasing can be resolved with increased depth sampling, but again at the cost of computational performance. For validation purposes the modes were chosen to be matched in this case, and the depth sampling was chosen for economy. The frequency of the highest order mode used was confirmed to be well below the Nyquist limit.

Both the normal mode and simplified models do well in predicting Lloyds Mirror interference in the near field, under 500 m. The simplified model shows excellent results in the intermediate field, here taken to be between 500 m and 1.5 km, while the normal mode model has difficulty predicting the exact location and depth of peaks and nulls. Moving into the far field region, over 1.5 km from the source, the simplified equation model increasingly over predicts the transmission loss. The divergence of the simplified equation model in the far field is to be expected from the isovelocity assumption, and in fact the same divergence was seen in Pedersons results for constant sound speed [26]. It is important to note that while the divergence is expected, its value can be difficult to predict, due to the effects of intense caustics and shadow zones caused by refraction. The normal mode model does comparatively well in the far field, on average under-predicting the experimental transmission loss by approximately 10 dB. It is however drastically noisier then the experimental results, fluctuating within a 25 dB range.

The noise present in the far field of the normal mode model can be explained by examining the formulation of the vertical water column. Pederson indicates that the vertical water column used in experiment had an average depth of 2200 fathoms, or approximately 4 km, and details on the sea floor boundary condition are not included. Computational restraints prevented the simulation of a 4 km water column, and so the data in figure 4.1 uses a 500 m deep column and assumes a stiff sea floor, modeled by a Neumann boundary condition. The formulation of sea floor boundary conditions in normal mode models is a complex topic requiring detailed knowledge of the experimental conditions, and will not be covered here. It can however have a significant impact on modeling results. A stiff sea floor can itself act as an efficient reflector, in the same manor as the sea surface, and thereby can cause a second Lloyd's

Mirror effect to be generated.

Figure 4.2 shows the results of formulating the simple source model so as to account for a perfect reflection from the sea floor. This sea floor reflection was accomplished with the addition of a third simple source term in the pressure equation,

$$p(r,z) = \frac{e^{ikR_1}}{R_1} - \frac{e^{ikR_2}}{R_2} - \frac{e^{ikR_3}}{R_3}, R_3 = \sqrt{r^2 + (2D - z - z_s)^2}. \tag{4.2}$$

From this model, far field noise similar to that predicted by the normal mode model can be observed. The transmission loss is also seen to diverge in the far field, suggesting that the presence of the sea floor decreases far field transmission loss. These results suggest that sea floor reflections will introduce noise into the far field predictions of the normal mode model, as well as decreasing the predicted transmission loss. Based on this evidence it is concluded that the predictions of the normal mode model are physically accurate for the assumed boundary conditions, but that the sea floor boundary condition itself is inappropriate for the problem.

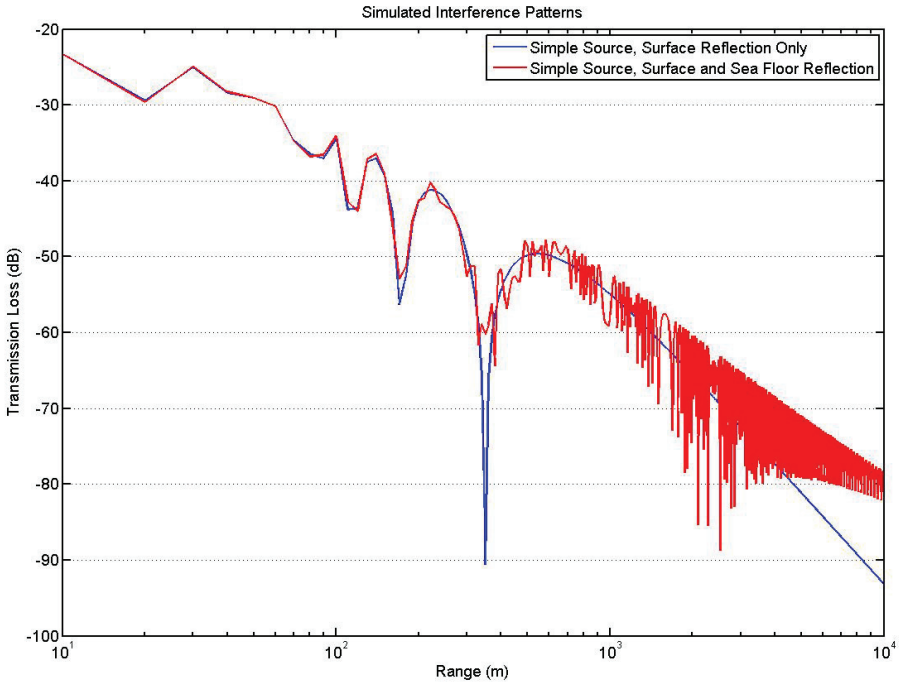

Figure 4.2: Simple Source Model representation of Lloyd's Mirror Including Sea Floor Reflection

Both of the models were able to replicate the unique character of Lloyd's Mirror interference in the intermediate field (its characteristic peaks and nulls), however

the simplified model was able to more accurately predict their location and value. In the far field, the simplified source model over-predicts the transmission loss, as expected for its finite sound speed assumption. The normal mode model however suffers from the effects of its sea floor boundary condition, causing it to predict a noisy far field, whose average transmission loss under-predicts the experimental value. Despite this noise, the normal mode model may still provides a more accurate estimate in the Lloyd's Mirror far field, depending on the horizontal range. For the purposes of simulating the sea surface Lloyd's Mirror effect, both models will be taken as adequate.

4.2 Simulation Setup and Trial Conditions

4.2.1 Experimental and Simulation Conditions

The simulation setup details remain the same as those presented in section 3.1. For the acoustic trials, recordings were taken using sonobuoys located of a depth of 90 ft. Two different ship aspects, or approach angles, were recorded in trials. The head aspect has the recording sonobuoy initially 1123 m from the bow, with the ship approaching head on. The beam aspect has the sonobuoy initially 644 m directly to port, with the ship maintaining course and passing the buoy. The ship speed is taken to be 10 knots in both aspects, and the sea state is again assumed negligible. The further assumption of a still ocean without any convection of sound by mean flow allows the CFD data for a given speed to be used for either aspect. Figure 4.3 shows diagram of the experimental setup for both aspects.

A static acoustic ranging of the Quest was performed prior to the dynamic ranging. Quest was placed on static moorings and its onboard machinery state varied while acoustic recordings were taken. By staggering the startup of various pieces of essential ship board machinery, and using various common machinery states, information on the operational noise of different pieces of ship board machinery could be gathered. These different components were then isolated and used to design a filtering envelope, with the goal of being able to accurately filter machinery noise out of dynamic ranging acoustic data. This process was carried out by DRDC specialists. A number of other steps were taken to remove ambient and propeller noise as well. The experimental

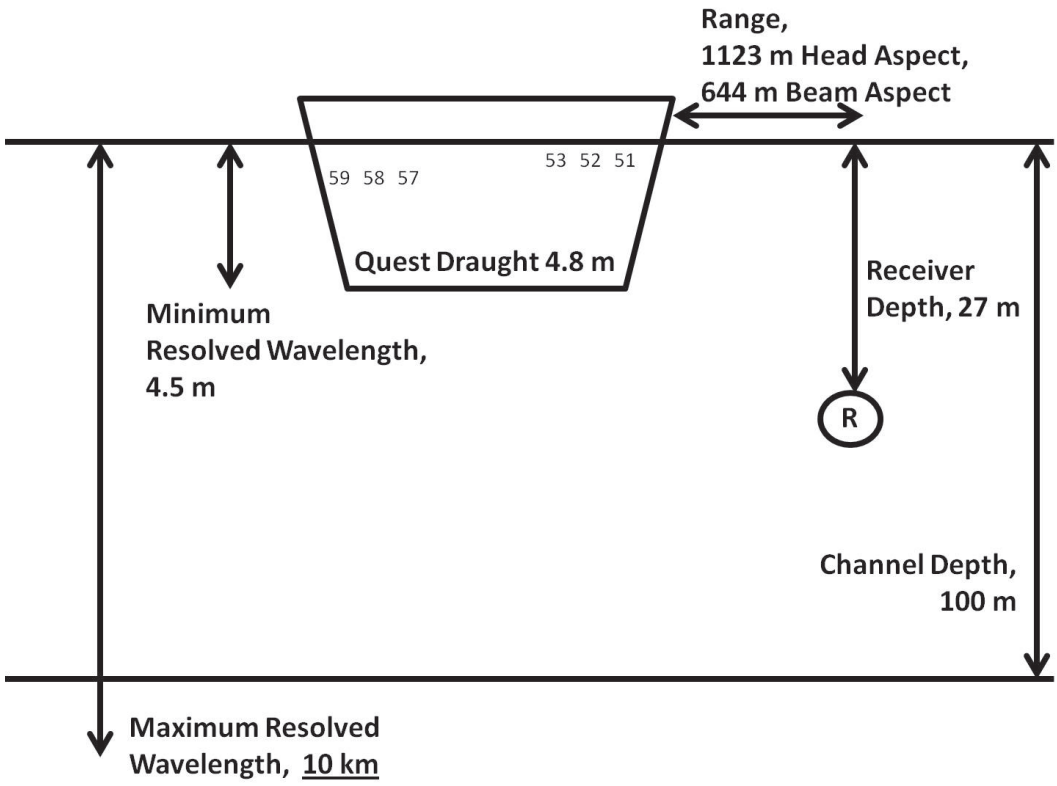

Figure 4.3: Geometric Setup of Acoustic Rangings of CFAV Quest

data in this chapter has therefore been filtered and conditioned. Due to security concerns the details of this filtering process and the raw unfiltered data are not able to be released. The experimental data presented in this chapter therefore represents a limited subset of the total acoustic data, and the accuracy of the experiment and details of the filtering process are not known.

4.2.2 Modal Parameters

The normal mode model requires additional information on the water column in order to achieve best results. A brief parametric study of the normal mode model was undertaken, using the same experimental data as in section 4.1 as a tuning case. The number of modes used and the sampling of those modes will be examined for their contribution to the final result. Various options for the sound speed gradient will also be discussed.

Figure 4.4 shows the results from the normal mode model with a varying number of modes. From theory, increasing the number of modes should increase the performance

of the model. However, care must be taken to ensure that the modes are adequately sampled so that the higher order modes are not subject to aliasing. Typically, the contribution of higher order modes will suffer from diminishing returns, as higher modes tend to be damped out over large ranges. Figure 4.4 shows a clear difference in the quality of the intermediate field prediction between 20 modes (blue) and 40 modes (red), however that difference is not as pronounced between 40 and 80 modes (green). These signals were produced with constant sampling for each, and therefore the 80 mode signal is most at risk of aliasing among its modes. A spectrum analysis indicated that all the modes are still below the Nyquist limit for the 80 mode signal, however they are several factors closer then those of the 40 mode signal. As more modes are included, the transmission loss tends to converge to a constant value in the intermediate field.

The 20 mode signal, while suffering from far less far field noise, does not accurately predict the depth of the nulls in the intermediate field. As the number of modes used increases, the depth of the nulls and their location becomes more accurate, however far field noise is also increased. As was shown in figure 4.2, the far field noise is believed to be a physical prediction that results from the assumption of a rigid sea floor, and not a numerical artifact originating from the mode sampling. From theory, higher mode numbers should be preferred at all ranges provided they have been adequately sampled. However, the results from 4.4 indicate that higher mode numbers are preferential only in the near and intermediate fields, in order to ensure resolution of the Lloyd's Mirror character. In the far field, higher mode numbers increase the noise introduced by the rigid sea floor assumption, to the detriment of far field predictions. For these reasons, the appropriate number of modes must be viewed as being dependent on the range of interest in the application.

Increasing the sampling ratio has little affect on the averaged results but does affect the noise in the signal. Figure 4.5 illustrates this result for 40 modes at varying sampling ratios. For readability of the plot, a 15 sample moving average filter was applied to the data to smooth the noise. A casual analysis of the data would seem to show that lower sampling ratios give better results. However, an analysis of the modes used at these lower ratios clearly shows that they have been undersampled. Obviously a minimum sampling ratio must be maintained in order to ensure that all modes used

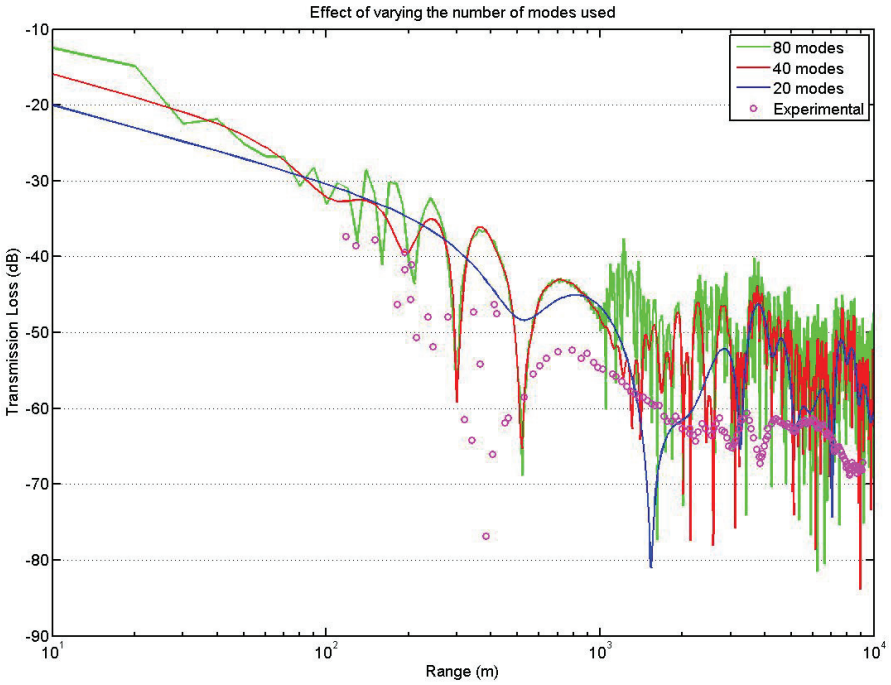

Figure 4.4: The effect of varying the number of modes used in the transmission loss approximation of the normal mode model

are adequately sampled, here between 0.5 and 1 samples/m. Beyond this point there is little to recommend one sampling ratio over the next, as they increasingly overlap. The moving average filter limits the ability to discern the character of Lloyd's Mirror interference from this plot, however analysis of the un-filtered data reveals its presence in the higher three sampling ratios, with negligible difference between them. Based on this, the major benefit of increasing the sampling ratio is simply increasing the number of adequately sampled higher order modes. It is concluded that so long as the sampling is adequate for the desired number of modes, little is gained by further increases.

The last parameter that must be supplied to the modal model is the sound speed gradient itself. The normal mode model was built such that the gradient must be supplied by the user, here four gradients will be explored. The character of the gradient will greatly affect the results, and will also largely determine the models response to variable depth and sea floor boundary conditions. Wherever possible this parameter should be determined from experimental data. However, such data is not

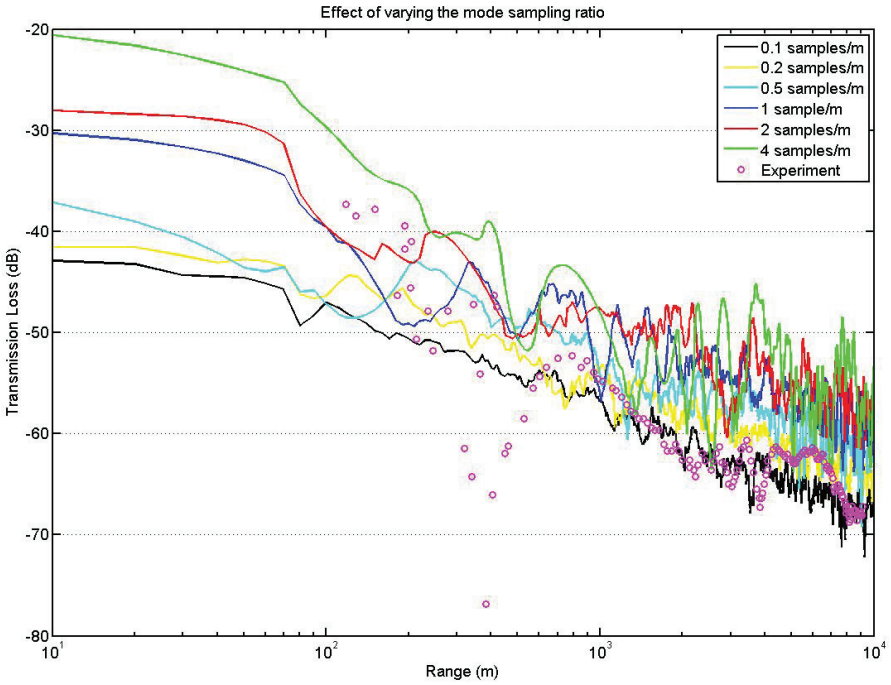

Figure 4.5: The effect of varying the mode sampling ratio on the simulation transmission loss

available from the acoustic trials conducted on CFAV Quest, and so the gradients used in the model have been taken from literature. Figure 4.6 gives the results from simulations using different sound speed gradients. For readability, the far field has been separated from the near and intermediate field in this figure, and a moving average filter of 10 samples width was applied to the far-field data only. The sound speed gradients are additionally plotted at the left of the figure.

The isovelocity gradient represented assuming that the ambient speed of sound is constant, in this case rounded to 1500 m/s. It is interesting to note that this case does not converge to the same result as the simplified equation model, not shown here, which also has a constant speed of sound. This difference is again due to the influence of the sea floor. The simplified equation model assumes an ocean of infinite depth with no sea floor effects. In reality this assumption is incorrect, and a number of effects can be caused by the sea floor, such as reflection and scattering.

The Munk profile is an idealized deep water profile commonly used for sea-surface

modeling problems in the deep ocean[22][15]. The Munk profile is given by the equation

$$c(z) = 1500\left[1 + \epsilon\left(\tilde{z} - 1 + e^{-\tilde{z}}\right)\right], \tag{4.3}$$

with $\epsilon = 0.00737$ and $\tilde{z} = \frac{2(z-1300)}{1300}$. Due to the 500 m depth chosen in this investigation, some of the Munk profiles deep water character is lost. The profile will change directions at a point specified in the depth scaling function. The shallower depth was chosen due to performance limitations of other profiles, and because the trials data is taken in shallower water. The Pederson profile is the bi-linear gradient given by equation 4.1, as above. Finally, the Hines profile is taken from experimental data reported for the Halifax area in the summer by Hines in [14]. The Hines profile data is reported up to a depth of 100 m, and has been extrapolated from there using the first derivative of the gradient at 100 m.

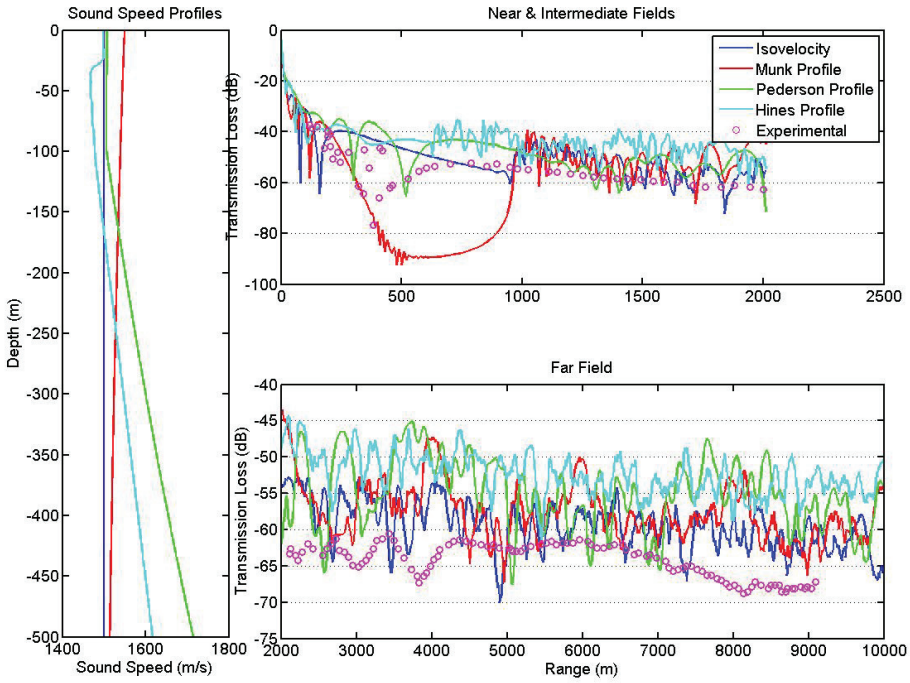

Figure 4.6: The result of normal mode model simulations with varying sound speed gradients

The performance of the different gradients is best broken down into the intermediate and near field, and the far field. In the near and intermediate field, none of the models is able to perfectly replicate the distinct null seen at 450 m. The Munk profile

is able to match its depth but then shows a marked gradual rise instead of the sharp increase that is characteristic of Lloyd's Mirror nulls. This rise is not duplicated in the other models or experiment. It is possible that it may be eliminated through the use of more, higher order modes, however, for the sake of comparison all models shown here use the same modal parameters (in this case, 500 modes used). The Pederson and isovelocity models both distinctly show the peaks and nulls, however neither model is able to accurately predict their depth or location. Finally, the Hines profile has some success predicting the location of the peaks and nulls, but cannot adequately predict their depth, especially in the case of the 450 m null.

In the far field, the models all continue the trend of under-predicting the experimental transmission loss. The isovelocity and Munk profiles perform best on average, within 5 to 10 dB of experimental on average, while the Hines and Pederson profiles are typically over 10 dB in error. None of the models shows any distinct advantages over the others; all show significantly more noise than is present in the experimental results, in which none of the oscillations that do appear are reflected in the simulation.

The isovelocity profile poorly reflects the physics of the real ocean due to its constant sound speed, and would seemingly add no physical realism to offset its complexity when compared to the simplified source or method of images, and so will not be considered. The Pederson profile represents a simplified profile that has been tuned using experimental parameters gathered for the validation case, and so it is expected that it will perform well in the validation case but not be generally applicable. On the other hand, while the Hines model gives poor results for the depth of the null in this case, it is important to remember that it is local to the Halifax area where the Quest trials took place. The Munk profile, while performing well in the far field, had wildly divergent results in the mid field region between 500 m and 1 km. For these reasons, the Hines profile is chosen for the simulation of the Quest trials. The channel depth is taken as 100 m so as to match the Hines profile data, and was sampled using 800 points. 400 modes was found to provide a reasonable balance between computational time and accuracy, while still ensuring that the highest order mode was adequately sampled.

4.3 Results and Discussion

Figure 4.7 displays the simulation results for the ship moving at 10 knots, head aspect, in a plot of sound pressure level or SPL versus Strouhal number. The original acoustic model, which does not include the effect of Lloyd's mirror interference is shown with dark blue, the experimental sea trials results are violet, while red, green and cyan represent the simple source, method of images, and normal mode models respectively. The results for the beam aspect simulation are given in figure 4.8.

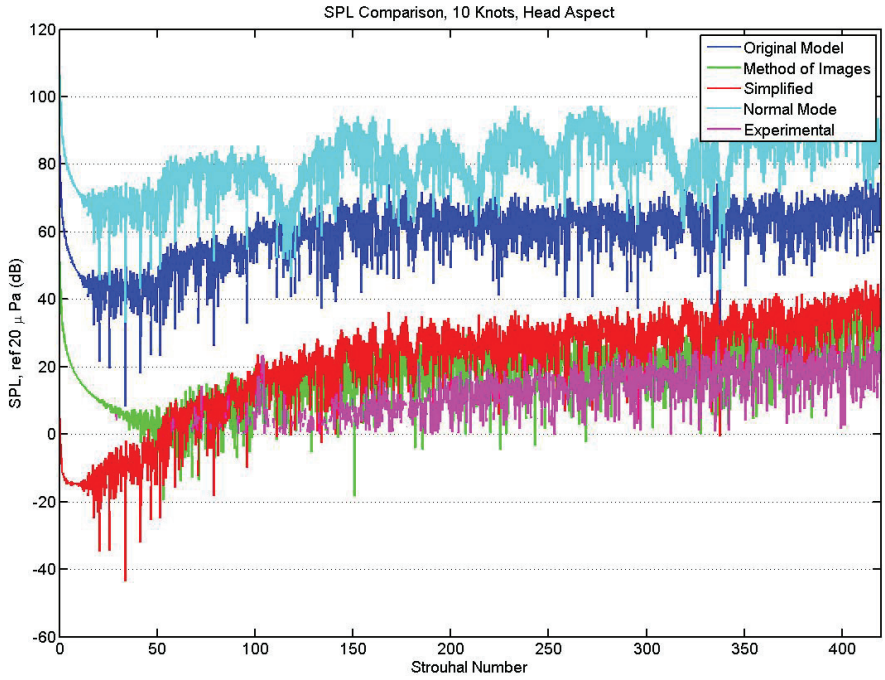

Figure 4.7: Acoustic Simulation Results, 10 Knots, Head Aspect

Table 4.1 summarizes the mean SPL from both cases. Both the simplified source model and the method of images give improved predictions compared to the original model. The simplified source model can be seen to improve the predictions of the acoustic post processor by approximately 35 dB, while the method of images can be seen to further improve predictions by 2.5 to 5 dB, for both aspects. In these cases the improvements are broadband in nature, with seemingly no dependence on Strouhal number. While it was not possible to validate the method of images against experimental results, it was seen in section 4.1 that the simplified source model can be

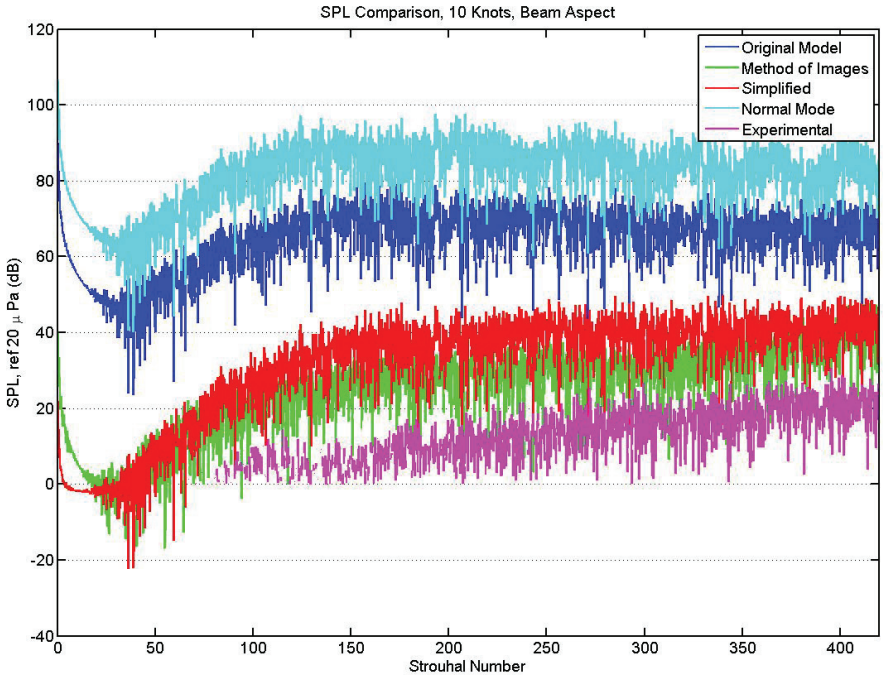

Figure 4.8: Acoustic Simulation Results, 10 Knots, Beam Aspect

expected to give good results for ranges under 2 km, in which both aspects are operating. Recall from chapter 2 that the method of images itself is utilized in the derivation of the simple source model; the essential difference between the two methodologies as implemented here is the assumption of a simple, acoustically compact source. It is expected that the method of images will have a similar performance envelope when compared to the simple source model. Based on its predictions relative to the validated simplified source model, it can be confidently concluded that the method of images also represents a valid, and improved, solution.

Model	Mean SPL ref $20\mu Pa$	
	Head Aspect (dB)	Beam Aspect (dB)
Original Model	58.7	64.2
Simple Source	20.2	30.6
Method of Images	17.7	24.9
Normal Mode	80.6	81.3
Experimental	12.8	14.8

Table 4.1: Mean Simulation Results, 10 knots

The results from the normal mode model are not as promising. It predicts significantly less transmission loss when compared to the other models, including the original, unaltered post processor, and in fact raises the observed SPL at the receiver by approximately 20 dB. A significant difference is seen in the character of the normal mode signal: unlike the simple source or method of images, the transmission loss from the normal mode model does not appear to be independent of Strouhal number. Several local minimums in the signal strength can be seen in figure 4.7, starting at $Str \sim 120$, and to a lesser extent in 4.8, starting at $Str \sim 300$. Identical trends were observed in section 4.1, where they were shown to be the result of incorrectly using the stiff sea floor boundary condition. It is likely that this is again the case, however without more detailed knowledge of the experimental environment, it is not possible to formulate a more physically accurate boundary condition.

The reader will note that none of the propagation models appear to display evidence of the pattern of peaks and nulls that was highlighted as being characteristic of Lloyd's mirror interference in chapter 2. The lack of peaks and nulls is not a failure of the models, but rather a result of the operating conditions. The depth of the ship as a source, in this case comparable to the draught of 4.8 m, is so small that it has the effect of practically eliminating the intermediate portion of the field. Both aspects are then operating in the far field for this geometry, where the surface reflection phase shift will dominate the travel time phase difference, and the two signals will be increasingly out of phase. The simple source and method of images models correctly predict increased transmission loss when compared to the spherical spreading case, in this study represented by the original unaltered model. In figure 4.2, the influence of the sea floor boundary condition was also shown to be a far field phenomenon, which increases the likelihood that the deficiencies of the normal mode model are caused by this assumption.

There are a number of potential sources of error that may explain the remaining gap between the predicted and experimental signals. While the addition of the Lloyd's Mirror effect is a step towards accurately modeling acoustic propagation, a number of additional propagation effects remain unaccounted for. Over longer ranges, absorption will play an increasing role in the transmission loss, as viscosity and other effects convert the acoustic energy into heat. The ocean is also largely non-homogeneous,

both vertically as discussed, but also horizontally. Non-homogeneity can be caused by chemical concentrations, such as localized salinity, currents, or the presence of undersea structures and life. While absorption is relatively easy to predict, horizontal non-homogeneity is very complex, and would require a detailed knowledge of the surroundings that is often not possible in experiments conducted at-sea.

The largest unaccounted for propagation effects will be the influence of convection, roughness of the surface, and the sea floor. All of the analysis conducted assumed a still ocean, which while ideal, is often not the case. Velocity fields in the water will cause the sound to be convected in the direction of the flow, which will change the received sound depending on the orientation of the receiver and the flow[15]. The presence of waves on the oceans surface will also impact its ability to reflect sound and create Lloyd's Mirror interference. Waves can be thought to roughen the ocean surface, and thus cause scattering and imperfect reflection[15]. While the trials conditions aimed for a small sea state to minimize convection, it is unlikely that a perfectly calm ocean was achieved. Trial logs [1] do not quantify the sea state beyond indicating "mild seas".

As is seen in the normal mode models predictions and figure 4.2, the sea floor can have a very large influence on acoustic propagation in shallow waters. Like the oceans surface, the sea floor can reflect sound, causing its own Lloyd's Mirror effect. It is however much more complex, in that its reflection characteristics will be determined by its composition. A smooth, hard sea floor made of rock would be a much more efficient reflector then one made of soft mud. Further to that, some sea floors will absorb and transmit the sound internally, possibly allowing it to re-enter the water column further downrange. It is possible, depending on the material, that this transmission may even be faster then propagation in the water. All of these factors combine to make modeling reflections from the sea floor much more complex than those created by the oceans surface [15],[10]. Figure 4.3 displayed a schematic diagram of the experimental geometry, including the minimum and maximum wavelengths captured by the simulation. Based on the 100 m depth, it is obvious the long wavelength sound would have significant interaction with the sea floor. None of this interaction was captured by the current models. Unfortunately, experimental data in the low wavelength range is unavailable, and the accuracy of simulations in this

range cannot be assessed. Despite this inability, 5he neglect of the sea floor and its effects is a significant source of model error.

Specific to the normal mode model is the error introduced by the assumed sound speed gradient. The gradient used in the analysis of CFAV Quest was an experimentally determined gradient reported by Hines in [14] as being "a typical profile for the region in summertime". While using a local gradient is beneficial, exact agreement with experimental conditions cannot be assumed. The trial's during which Quest's signature was measured took place in mid October in the Halifax area, and due to the expected seasonal variation of sound speed profiles, are not expected to match. Further, the profile was extrapolated from 100 m depth to 500 m depth, the validity of which is unknown. The assumed profile must therefore represent a potential source of error. Figure 4.6 examines the sensitivity of the normal mode model to different gradients, and it was seen that while there is significant sensitivity to the gradient in the near and intermediate field, the far field variation was within 10 dB for every gradient inspected. While this remains a source of error in the normal mode model, it is not expected that this assumption can account for all of the error seen in the normal mode model.

As with the pressure data, it is difficult to quantify the experimental error for the acoustic results. Security concerns prevent the release of either the unfiltered acoustic signal or the details of the filtration process. As Murphy discussed in [23], it is more likely that the filtration process would remove desirable signal elements then fail to remove undesirable ones, however a measure of the experimental error remains unquantifiable by the author.

Finally, it is important to realize the limitations of the two stage modeling process, and the errors that may be introduced by the CFD process. Chapter 3 highlighted the accuracy of predictions of pressure fluctuation in the CFD data, and showed that not only was pressure fluctuation significantly under predicted in six sensors mounted on the hull, but also that this under prediction could potentially have a large impact on the acoustic simulations. Several of the sources of modeling error that were deemed significant to the CFD computation would also be significant to the acoustic generation and propagation.

The wave system generated by the ship's motion would generate and propagate

noise, however this effect has been entirely neglected. This constitutes a significant modeling error in both the CFD and acoustic stages of the modeling. The bow and stern waves would significantly alter the flow field on the ships hull, and would certainly change the character of noise generated. Furthermore, the ship would radiate surface waves, which would themselves both generate noise and alter the character of sound propagating through them. By neglecting the free ocean surface and the stern portion of the ship, a large degree of modeling error is introduced.

Unfortunately, despite the results of the acoustic simulations, the impact of the CFD error is still ambiguous. While the CFD pressure fluctuations were shown to under predict those detected experimentally, the accuracy of the predicted stress field is unknown. It is possible that the noise generation may be dominated by the stress field, which may or may not be more accurate then the pressure. The error in the pressure field was also seen to be dependent on location. Due to the low spatial fidelity of the experimental setup, it is not possible to determine the accuracy of the entire fluctuating pressure field. Without further testing in a more detailed and controllable environment, it is not possible at this time to quantitatively discuss the impact of errors introduced by the CFD calculation.

4.4 Chapter Summary

In this chapter the simple source and normal mode models were validated, and in the case of normal mode, tuned, using experimental results. All models were able to accurately recreate the peaks and nulls that defined Lloyd's Mirror interference, however in the validation and later the predictions for CFAV Quest, all the models ran into difficulties in the far field. The method of images and simplified source models both performed well at ranges under 2 km, and gave significantly improved predictions compared to the original model. As the transmission range was increased to over 2 km, both the method of images and simple source models increasingly over predicted the transmission loss as the assumption of a homogeneous transmission medium broke down. Conversely, at the same ranges the normal mode model under-predicted the transmission loss, as well as incorrectly predicted a high degree of spectral noise. These features were reproducible in the simple source model by assuming a reflecting sea floor, and so they are believed to be physical predictions due to the assumption

of that boundary condition in the normal mode model.

Comparisons with results from at sea trials show that both the simple source model and the method of images gave significantly improved results when compared with the original acoustic post processor. As expected from the validation, the normal mode model compared poorly in comparison. The trials ranges were all within the far field, a range at which none of the models is optimum.

While the results from the method of images and simplified source models are very similar, the method of images is the superior model. It removes some of the simplifying assumptions used by the simple source model, and gave improved predictions for the sound generated by CFAV Quest at 10 knots in both aspects. It is expected that if this analysis were extended to higher Strouhal numbers the advantage of the method of images would increase, as the acoustic compactness assumption of the simple source model becomes increasingly inaccurate.

While the effect of Lloyd's mirror interference can be significant, it is not the only element of propagation physics in which the acoustic post processor was lacking. Acoustic interactions with the sea floor can have a similar effect as Lloyd's Mirror interference. Additional propagation phenomenon, such as absorption, as also not accounted for in any of these models. It is also worth noting that the results from the normal mode model could be significantly improved with more knowledge of the experimental conditions, including the composition of the sea floor and the local sound speed gradient. The normal mode model presented here is a very simple implementation of a complex model frequently used to great effect in computational acoustic oceanography, and should not be discounted for future improvements and applications. Finally, while some improvements on the acoustic predictions could be gained by the addition of more acoustic propagation physics, it is unlikely that all of the error seen here can be attributed to its lack. Further investigation is needed to determine the nature and impact of errors introduced into the acoustic prediction by the CFD calculations.

Chapter 5

Conclusions and Recommendations

5.1 Conclusions

The over arching goal at each stage of the modeling process presented herein has been accurate prediction of the hydrodynamic hull noise of CFAV Quest. To this end it was hypothesized in chapter 1 that a model capable of simulating the Lloyd's mirror effect of the ocean surface would improve upon the predictions of the Lighthill-Curle acoustic analogy. It was also undertaken to further validate the combined simulation process through an analysis of the NWT's predictions for fluctuating hull pressures.

In chapter 2, the development of three different acoustic propagation models that could predict the transmission loss due to Lloyd's mirror was presented. These models represented in turn an increasingly realistic set of assumptions about the underlying acoustic propagation physics, with a corresponding increase in complexity. The simple source model approximated the ship as an acoustically compact source in a linear medium and solved for the transmission loss such a source would experience. The method of images utilized a very similar derivation, but removed the restriction of an acoustically compact source and instead solved the Lighthill-Curle acoustic analogy equation with a method of images solution. To the authors knowledge, such a solution to the problem of sound generation in the vicinity of a reflecting half plane has not previously been attempted, and so the method of images solution represents a significant contribution to the field of hydroacoustics. Finally, the normal mode model sought to further remove the requirement of a linear or homogeneous medium, by solving for the inhomogeneous water columns response to acoustic excitation.

These models were validated in chapter 4, and their results compared with data obtained from at-sea trials of CFAV Quest. Both the simple source and method of images models were shown to significantly increase the accuracy of predictions in both head and beam aspects, with best results coming from the method of images. This trend is expected to continue for all ranges at which the assumption of a homogeneous

ocean is valid, typically on the order of 2 km.

The normal mode model, which was developed for its advantages in the far field, did not perform as expected. In validation tests its accuracy in the near and intermediate fields was fair, if not as good as the method of images or simple source. However, it significantly under-predicted the transmission loss in the far field. Results from the normal mode model of CFAV Quest predicted sound pressure levels that were in fact higher then those predicted by spherical spreading. This deficit is believed to be due to assuming a stiff, solid sea floor boundary condition for the water column.

Finally, in chapter 3, the fluctuating component of hull pressure was compared between the simulated flow field and that recorded in experimental trials of CFAV Quest. The disagreement between the two pressure signals was significant. The accuracy was shown to be proportional to the ships speed and inversely proportional to the frequency of interest. The error was also seen to be geometrically distributed, with those sensors at the extreme fore and aft ends of the simulated ship having the worst accuracy. Pressure fluctuation is one of several factors in noise generation, and a simple sensitivity study of the acoustic model showed that this pressure error would affect the accuracy of the acoustic simulations.

Based on these results, a number of conclusions can be made. The validation of the simulated pressure fluctuations revealed significant error in the CFD model. These errors will propagate into the acoustic solutions, and must be resolved in order to have confidence in the acoustic predictions. The one-way coupling of the acoustic solution with the flow field solution requires the turbulent flow field to be well simulated, and so an accurate CFD solution is critical for acoustic predictions. A number of sources of error were highlighted, including turbulence modeling, the lack of a free surface model or bow wave, and the choice to model only the bow half of the ship. Recommendations for addressing these errors will be put forward in the following section.

The major goal of the acoustic models in this work was to accurately capture the Lloyd's Mirror effect of the sea surface, and in that, all three models succeeded. Despite the uncertainty of the CFD computation, the simple source model and method of images solution were shown to improve far-field predictions, on average by 36.5 dB and 40.2 dB respectively. The best acoustic results for all cases studied were obtained

from the method of images. The added complexity of a method of images solution is minor, simply requiring the Lloyd's mirror calculations to be repeated for the image ship. While this necessarily requires an approximate doubling of the computational time in the acoustic post processor, the length of acoustic computations is dwarfed by the CFD calculations. A method of images solution to the Lighthill-Curle acoustic analogy will improve accuracy for acoustic predictions near a reflecting half plane like the ocean surface, with minimal increase in model complexity and cost. It also constitutes a novel new method for calculating the hydrodynamic hull noise generated in the vicinity of a reflecting half plane. For these reasons, a method of images solution to the Lighthill-Curle acoustic analogy is recommended for all future hydroacoustic calculations in which the reflections from the ocean surface are a significant factor, and a linear medium can be safely assumed.

For higher range problems, a method of images solution would still be in error due to the assumption of a homogeneous ocean. In such cases, a non-linear model such as the normal mode model must be considered. Such models can give significantly improved predictions compared to ones which assume a constant velocity, so long as all the details of the medium are properly accounted for. Due to a lack of knowledge about experimental conditions during the acoustic trials, a number of details such as sea floor boundary conditions and sound speed gradient had to be assumed. These assumptions were shown to significantly and detrimentally effect the predicted transmission loss. By replacing these assumptions with measured values, a significant increase in accuracy is likely possible.

5.2 Recommendations

Two distinct paths are available for further progress on the acoustic modeling methodology: further refinement of the CFD calculation, and expanding the acoustic model to include more realistic propagation. Numerous additional improvements to the predictive power of the acoustic post-processor are possible. Acoustic propagation in the ocean is a complex subject, and a number of physical processes remain un-accounted for in the present model. Acoustic interactions with the sea floor can be extremely important in shallow water problems. At long ranges, phenomenon such as acoustic absorption and dissipation by viscosity can also become significant. At extreme

ranges, the effect of refraction due to gradients in the speed of sound become important, and any model making predictions at these ranges would have to take this into account, such as was attempted in the normal mode model. A fully developed propagation model would be able to account for all of these effects, and would provide significantly more accurate predictions for those cases where they are important.

The improvement offered by these models is directly tied to the ability to describe the ocean as an acoustic medium. As was seen in the normal mode model, expansion of the acoustic propagation models requires increasing amounts of information about the experimental environment. This necessarily increases the cost of validation experiments, while at the same time specializing the models to specific applications. As they specialize, they will also grow in complexity, and likely suffer from diminishing returns in terms of prediction improvements in dB. Further, it was seen that there is significant error being introduced into the modeling process by the CFD calculations. The tiered modeling approach means that that error will propagate through and potentially overwhelm any further improvements made to the acoustic models.

Improvements to the flow field predictions could be obtained through a variety of approaches. A grid convergence study has thus far not been attempted, and the discretization error cannot be quantified. As a result, it is not currently known if the mesh resolution is adequate to ensure a good representation of the flow field. The model of CFAV Quest used here has been simplified by cutting it in half and placing an end cap on the mid ship. This potentially introduces several sources of error as was discussed in section 4.3. While time consuming, both of these steps are straight forward in implementation, and offer significant potential.

Additionally, the hybrid Baldwin-Lomax-Smagorinsky turbulence model constitutes another avenue for improvement, due to its tendency to produce physically inaccurate results in the near-wall regions of interest in this study. New cutting edge turbulence models have evolved using a similar framework to hybrid LES models, known collectively as detached eddy simulation or DES. These models aim to marry the resolution of large eddy motion from LES with the use of turbulence transport equations to model the sub-grid scales. The addition of a more state of the art turbulence model has the added advantage of being a widely applicable improvement to the NWT, beyond its application to hydro-acoustics.

Finally, the NWT is currently incapable of modeling a free surface boundary condition for the flow around the ship, and so must instead assume a constant slip wall. This assumed boundary condition is physically inaccurate, and a major source of modeling error. A consequence of this lack is the inability to solve for the waves at the bow and stern that would be generated by the ship in motion. These waves will not only effect hull pressure distributions that generate noise, but also the propagation of noise itself into the far field. By neglecting this set of phenomenon, significant modeling error is introduced into the process. While the addition of free surface effects into CFD models is not a simple undertaking, it would be a significant step towards a more well-formulated problem.

Bibliography

[1] Chief scientists log, q309. DRDC Internal Document, 2007.

[2] Cruise plan q-309. DRDC Internal Document, 2007.

[3] N. Alin, R.E. Densow, C. Fureby, T. Huuva, and U. Svennber. Current capabilities of des and les for submarines at straight course. *Journal of Ship Research*, 2010.

[4] J. Ask, L. Davidson, H. Enwald, and J. Larsson. An acoustic analogy applied to incompressible flow fields. *Computational Aeroacoustics: From Acoustic Sources Modeling to Far-Field Radiated Noise Prediction Colloquium EUROMECH 449: December 9-12, 2003, Chamonix, France*, 2003.

[5] J.S. Baggett. On the feasibility of merging les with rans for the near-wall region of attached turbulent flows. *Center for Turbulence Research Annual Research Briefs*, 1998.

[6] T. Bell. The numerical wind tunnel: A three-dimensional computational fluid dynamics tool. Master's thesis, Dalhousie University, 2003.

[7] F. Camelli and R. Löhner. Combining the baldwin lomax and smagorinsky turbulence models to calculate flows with seperation regions. *AIAA Aerospace Sciences Meeting and Exhibit, 40th, Reno NV US*, 2002.

[8] D.G Crighton. *Computational Aeroacoustics*, chapter 3: Computational Aeroacoustic for Low Mach Number Flows, pages 50 – 68. New York: Springer-Verlag, 1993.

[9] N. Curle. The influence of solid boundaries upon aerodynamic sound. *Proceedings of the Royal Society of London. Series A, Mathematical and Physics Sciences 231*, pages 505–514, 1955.

[10] P.C. Etter. *Underwater Acoustic Modeling: Principles, Techniques and Applications*. Elsevier Applied Science, 1991.

[11] J.B. Freund, S.K. Lele, and M. Wei. The robustness of acoustic analogies. *Stanford Center for Turbulence Research, Proceedings of the Summer Program*, 2004.

[12] C. Fureby and H. Almström. Hydrodynamic noise produced by the turbulent flow around a rigid hull. *Swedish Defense Research Agency, Base Data Report*, 2001.

[13] M.E. Goldstein. A generalized acoustic analogy. *Journal of Fluid Mechanics*, 2003.

[14] P.C. Hines and D.D. Ellis. High-frequency reverberation in shallow water. *IEEE Journal of Oceanic Engineering*, 1997.

[15] F.B. Jensen, W.A. Kuperman, M.B. Porter, and H. Schmidt. *Computational Ocean Acoustics*. AIP Press Series in Modern Acoustics and Signal Processing, 1994.

[16] M. Kaltenbacher, M. Escobar, S. Becker, and I. Ali. *Computational Acoustics of Noise Propagation in Fluids - Finite and Boundary Element Methods*, chapter Computational Aeroacoustics based on Lighthill's Acoustic Analogy, pages 115–132. Springer Verlag, 2008.

[17] J. Larsson, L. Davidson, M. Olsson, and L.E. Eriksson. Aeroacoustic investigation of on open cavity at low mach number. *Proceedings of the 9th AIAA/CEAS Aeroacoustics Conference and Exhibit: May 12-14, 2003, Hilton Head, SC*, 2003.

[18] M.J. Lighthill. On sound generated aerodynamically. part i, general theory. *Proceedings of the Royal Society of London. Series A, Mathematical and Physical Sciences 211*, pages 564–587, 1952.

[19] G.M. Lilley. The radiated noise from isotropic turbulence with applications to the theory of jet noise. *Journal of Sound and Vibration*, 1996.

[20] S. Marburg. *Computational Acoustics of Noise Propagation in Fluids - Finite and Boundary Element Methods*, chapter 11: Discretization Requirements: How Many Elements per Wavelength are Necessary?, pages 309–332. Springer Verlag, 2008.

[21] A.F. Molland. *The Maritime Engineering Reference Book: a guide to ship design, construction and operation*. Butterworth - Heinemann, 2008.

[22] W.H. Munk. Sound channel in an exponentially stratified ocean with applications to sofar. *Journal of the Acoustic Society of America*, 1974.

[23] S. Murphy. Predicting the hydrodynamic acoustic signature of canadian forces auxillary vessel quest. Master's thesis, Dalhousie University, 2008.

[24] N.V. Nikitin, F. Nicoud, B. Wshistho, K.D. Squires, and P.R. Spalart. An approach to wall modeling in large-eddy simulations. *Physics of Fluids*, 2000.

[25] A.V. Oppenheim and R.W. Schafer. *Digital Signal Processing*. Prentice-Hall, 1975.

[26] M.A. Pederson. Comparison of experimental and theoretical image interference in deep water acoustics. *The Journal of the Acoustical Society of America*, 1962.

[27] M.A. Pederson and D.F. Gordon. Normal mode theory applied to short-range propagation in an underwater acoustic surface duct. *The Journal of the Acoustical Society of America*, 1965.

[28] R. Pozo. Template numerical toolkit: An interface for scientific computing in c++. National Institute of Standards and Technology, Mathetmatical and Computational Sciences Division, March 2004.

[29] D. Ross. Mechanics of underwater noise, 1987.

[30] M. Wang, J.B. Freund, and S.K. Lele. Computational prediction of flow-generated sound. *Annual Review of Fluid Mechanics*, 2006.

[31] D.C. Wilcox. *Turbulence Modeling for CFD*. D C W Industries, 1998.

[32] J.E. Ffowcs Williams and D.L. Hawkings. Sound generation by turbulence and surfaces in arbitrary motion. *Philosophical Transactions of the Royal Society of London A*, 1969.

[33] N. Zhang, H.C. Shen, and H.Z. Yao. Numerical investigation of the flow induced noise of submarines. *Proceedings of the 8th International Conference on Hydrodynamics, Nantes, France*, 2008.

Appendix A

Welch's Method

Welch's method of power spectrum estimation is a popular alternative to the periodogram for determining the power-spectral content of a signal. In the most common method of spectrum estimation (known as the periodogram or sometimes referred to as simply "taking the FFT"), the Fourier transform is calculated from the finite signal $x(n), 0 \leq n \leq N-1$ by

$$X(e^{j\omega}) = \sum_{n=0}^{N-1} x(n)e^{-j\omega n} \tag{A.1}$$

using a Fast Fourier Transform algorithm. The spectrum estimate of the signal, $I_N(\omega)$ can then be calculated as

$$I_N(\omega) = \frac{1}{N}|X(e^{j\omega})|^2 \tag{A.2}$$

.

Welch's method instead sections the original signal into $K = N/M$ segments of length M. Segments can be chosen to overlap. These segments are then convoluted with an appropriately chosen window $w(n)$. These windowed segments are then Fourier transformed individually,

$$J_M^{(i)}(\omega) = \frac{1}{MU}\left|\sum_{n=0}^{M-1} x^{(i)}(n)w(n)e^{-j\omega n}\right|^2, i = 1, 2, ..., K, \tag{A.3}$$

with

$$U = \frac{1}{M}\sum_{n=0}^{M-1} w^2(n), \tag{A.4}$$

and the spectrum estimate is obtained by averaging the windowed segments,

$$I_M(\omega) = \frac{1}{K}\sum_{i=1}^{K} J_M^{(i)}(\omega). \tag{A.5}$$

.

The practical effect of this method is to reduce the variance of the spectrum estimate and smooth noise from the signal, at the cost of a reduction in spectral resolution. Different windows can be chosen and will have impacts on bias and smoothness of the resulting estimate. The Hamming window used in this study is given by the equation

$$w(n) = 0.54 - 0.46\cos\left(2\pi\frac{n}{N}\right), 0 \leq n \leq N \tag{A.6}$$

and is shown in figure A.1. Figure A.2 shows a comparison of the spectrum estimate

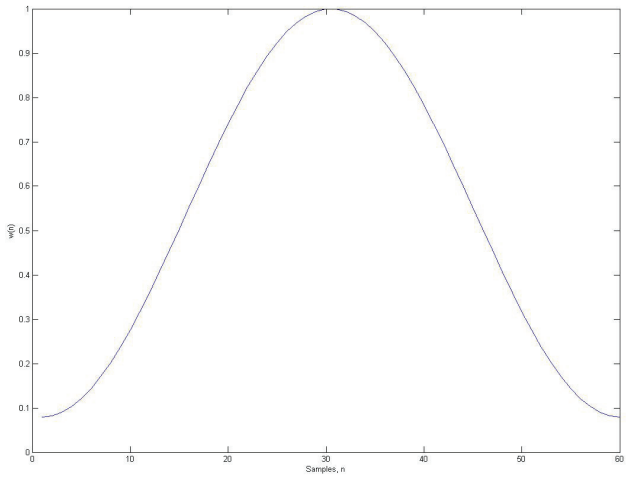

Figure A.1: A Hamming window for a 60 sample segment

given by a periodogram to that given by Welch's method. The Welch estimate uses the same windowing parameters as used in this study. There is a clear difference in both the noise, and the mean value of the estimates. The details are not presented here, but it can be shown that the periodogram has a higher estimation bias compared to Welch's method, and so is less accurate. For a more detailed analysis of the strengths and weaknesses of the techniques, see [25].

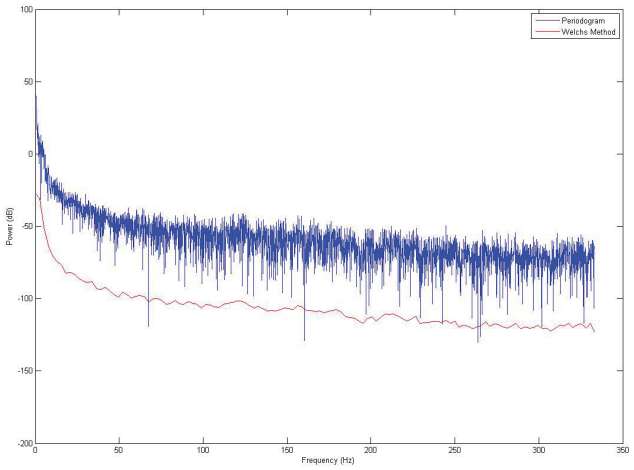

Figure A.2: A comparison of the periodogram to Welch's method for a signal

Appendix B

Viewing NWT Data within Matlab

Previous work by Murphy in [23] utilized the OpenDX and ParaView programs in conjunction with Matlab to analyze and visualize the data produced by the NWT. A secondary result of the work presented herein has been the development of a suite of Matlab routines that allow NWT data to be analyzed and visualized in Matlab alone. What follows is a users guide to these routines. For brevity, code will not here be reproduced.

NWT flow data is solved on an unstructured, anisotropic grid. Within the NWT this grid is stored as an unstructured list of all the cells in the current domain, and their reagent variables. This list can be output at frequencies specified by the NWT user. Rather then code a new output function into the NWT itself, the Matlab scripts were coded to use the same outputting format as OpenDX.

For every time step of interest, the NWT will output three binary files, which will be named for the timestep, with the addition of one of three notifiers: .pos, .con, or .dat. A full filename will then be "step0001.dat.bin" for example. Combined, the .pos and .con files describe the grid geometry, while the .dat file contains the flow data stored on that grid. All data stored in these files is saved as 32 bit floats or unsigned integers, depending on the data in question.

The .pos file will contain an M x 3 matrix, where M is a number related to the number of cells and their refinement. Each row describes a single vertex of one cell in the simulation domain. Due to the anisotropic refinement, the number of cells which contain a given vertex will be non-constant, and it is not possible to tell the number of cells from the number of vertices.

The .con file then contains an N x 8 matrix, where N is the number of cells. Each row of this matrix corresponds to one cell in the simulation domain, and each column entry gives the row index of one of the vertices of this cell. Since the grid is unstructured, these cells will not be ordered of themselves, however their order is

important for the index references of the .dat file. The same is true of the .pos file; the individual vertices are not meaningfully ordered, however changing their order would invalidate the indices of the .con file.

Finally, the .dat file contains all of the flow data. It contains an N x 3 matrix of flow velocity vectors for each cell, an N x 1 vector of pressures, and an N x 1 vector of cell ranks. The rank information relates to grid adaptation, and is of little use for flow data analysis.

The first step for any matlab application of the NWT data will be the *importAfter-solve.m* module. This module contains a series of functions for importing the three files described above for any given timestep. The timestep should be supplied to the function without file type suffixes, as in simply "step0001"; if the timestep required is not contained in the current working directory, the path must be supplied as well. If an .stl geometry is required as well, an identical process is required, and the function *import_stl.m* is used. It uses the .pos and .con data output by NWT for the .stl geometry, and if they are not in the working directory, the path must be provided to the function.

Once the data is imported into Matlab, the grid may be viewed at any time using the *createGrid.m* function. This function takes the geometry data and formats it so that it is compatible with the Matlab patch command. The patch command is built into Matlab, and can be used to visualize 3D objects by constructing them out of facets or 'patches'. The *createGrid.m* commands formats the grid data such that each cell is constructed of 6 of these patches, one for each face. It returns an array of faces that, when sent to the patch command along with the vertex data in the pos array, will allow it to plot the grid. The entire grid need not be formatted, by sending subsections of the con array, smaller sub-domains can be formatted and viewed. In conjunction with the *grid_search.m* command (discussed below) this can be used to view specific areas of interest on the grid.

Some simple analysis functions have been created. In order to explore the data contained on the grid, the user must first define the subset of data they're interested in. The *grid_search.m* function receives as input three vectors x,y, and z which describe parts of the domain. These vectors are used as targets to search the grid against, the function will return a matrix containing the indexes for the subset of the grid which

contains the points described by vectors x,y and z.

It is important to note that a given point in three dimensional space may have up to 8 cells which contain it, depending on whether that point lies within a cell, or on a cells face, edge or vertex. The function *pathfinder.m* takes the subset of cells found by the *grid_search.m* function and reduces it such that a given point corresponds to only one cell. It currently preferentially chooses the cell closest to the origin. The user is free to set the resolution of the vectors x,y and z as high as they like, however no interpolation of the data is done by these routines, they simply assign each entry of the vectors to a cell.

A number of simple plotting routines have also been provided. The pathfinder function outputs several variables which describe the dimensionality of the requested sub-domain. These variables can be passed to the *NWT_plot.m* function to generate simple plots. These functions are currently limited in their geometric capabilities. Lines must be straight and parallel with one of the cartesian basis vectors $\hat{i}, \hat{j}, or \hat{k}$, and planes must use two of them as their basis. Analysis for more complex geometries must be done on a case by case basis.

Appendix C

Additional Figures

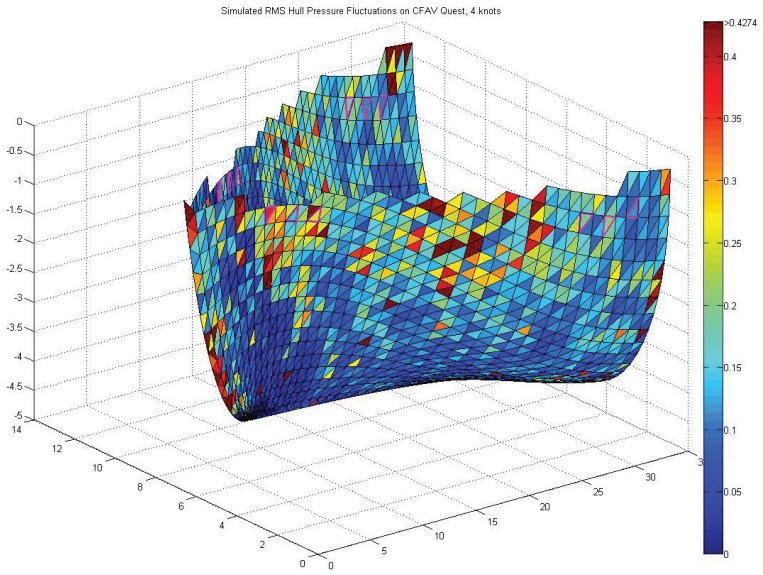

Figure C.1: Simulated RMS hull pressure fluctuations at 4 knots (kPa)

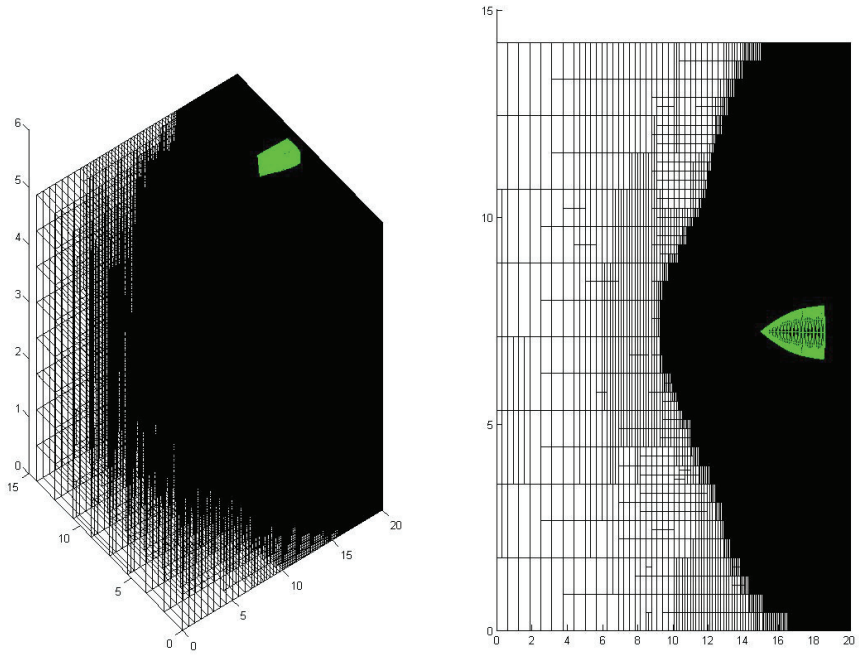

Figure C.2: Sample NWT Grid from 6 knots, 3D view and top down view